

**A THEORETICAL STUDY OF THE ENTRY OF BACULOVIRUS INTO CELL
NUCLEUS**

by

Roza Vaez Ghaemi

B.Sc., Amirkabir University of Technology, 2011

M.Sc., University of Tehran, 2014

A THESIS SUBMITTED IN PARTIAL FULFILLMENT OF
THE REQUIREMENTS FOR THE DEGREE OF

MASTER OF APPLIED SCIENCE

in

THE FACULTY OF GRADUATE AND POSTDOCTORAL STUDIES
(Biomedical Engineering)

THE UNIVERSITY OF BRITISH COLUMBIA
(Vancouver)

September 2016

© Roza Vaez Ghaemi, 2016

Abstract

The nucleocapsids of the baculovirus have been observed to undergo intracellular trafficking driven by actin polymerization. Propelled by an actin tail through the cytoplasm, the baculovirus nucleocapsid finds its way to the nucleus of the host cell. Then it docks to the cytoplasmic filaments of the nuclear pore complex (NPC), and manages to enter the nucleus intact. These interesting experimental observations inspired the current research. We first focus on the actin polymerization mechanism and the propulsive force generated at the back of the virus. Then, at the NPC interface, we integrate the mechanism for opening the central channel and passage of the virus. For the first part, using a microscopic approach and implementing an elastic Brownian ratchet model, we suggest a biphasic force-velocity relationship for baculovirus riding on the actin comet tail, which stalls at an external force of around 50 pN. Then, having this force value as the key parameter, we evaluate the idea of mechanical breakthrough into the NPC channel. For this purpose, we model the central channel of the NPC as saturated hydrogel. A mechanical fracture model shows that in order for the actin force to affect a purely mechanical breakthrough, the gel must be exceedingly soft. Although our results do not offer direct support for the hypothesis of a purely mechanical entry, they do not disprove the idea, either. Possibly the homogeneous hydrogel model for the NPC is inadequate, and more complex models (e.g. polymer brushes and forest) need to be examined. It is also possible that the mechanical entry of the virus is aided by biochemical signals that soften or partially remove the NPC barrier.

Preface

This thesis entitled “A theoretical study of the entry of baculovirus into cell nucleus” presents the research that I performed during my MASc study. The research conducted in this thesis was identified, initiated and supervised by Professor James J. Feng. In this preface, the contributions and collaborations to the published or submitted works are briefly explained.

A version of first part of this study was presented as a poster in the 12th annual northwest biomechanics symposium on June 2016 in UBC. The work was entitled “A Biomechanical Model for Baculovirus Propulsion Based on Actin Polymerization In Its Wake” by me, Brian Merchant and James J. Feng. In this poster, I developed the numerical model, performed simulations and collected data. The analysis was done by me and Professor James J. Feng together. I prepared the first draft of the poster which was later revised by Prof. Feng.

Table of Contents

Abstract.....	ii
Preface.....	iii
Table of Contents	iv
List of Tables	vii
List of Figures.....	viii
List of Abbreviations	xi
Acknowledgements	xii
Dedication	xiii
Chapter 1: Introduction	1
1.1 Motivation and objectives of this thesis.....	1
1.1.1 Characterization of actin propulsion for Baculovirus.....	2
1.1.2 Elucidation of a potential role of phenylalanine-glycine (FG)-Nups in the nuclear import of the virus.....	3
1.1.3 Evaluating the properties of the NPC central channel	3
1.1.4 Evaluating the mechanical entry hypothesis.....	4
Chapter 2: Literature review	5
2.1 Baculovirus: The largest virus replicating in the nucleus of the host cell	5
2.1.1 Structure and life cycle	5
2.1.2 Baculovirus applications.....	6
2.1.3 Intracellular trafficking of baculovirus	7
2.1.4 Nuclear envelope in viral infection.....	8

2.2	Actin polymerization	8
2.2.1	Macroscopic approach	12
2.2.2	Microscopic approach.....	13
2.2.2.1	Free filament-end models	14
2.2.2.2	Protein-associated models.....	16
2.2.3	Mesosopic approach.....	19
2.3	Nuclear pore complex	23
2.3.1	Mechanism of transport through the NPC	25
2.3.2	Models on NPC structure and functionality.....	26
2.3.2.1	Polymer Brush or Virtual Gating model.....	27
2.3.2.2	Saturated Hydrogel or Selective Phase model	27
2.3.2.3	Hybrid or Forest model.....	28
Chapter 3: Actin-based locomotion of the Baculovirus.....		32
3.1	Model set up.....	32
3.2	Model parameters.....	37
3.3	Model predictions	40
Chapter 4: Nucleus entry of the baculovirus.....		44
4.1	Deep penetration of a punch into a soft solid	45
4.1.1	Penetration of flat-ended punch	45
4.1.2	Penetration of sharp-ended punch.....	48
4.2	Baculovirus penetration into the soft gel on NPC central channel	50
4.2.1	Blunt conical tip baculovirus	50
4.2.2	Blunt conical tip baculovirus – modified model.....	52

4.2.3	Sharp conical tip baculovirus.....	53
4.3	Mechanical properties of the NPC gel	55
4.3.1	Shear modulus of the NPC gel.....	55
4.3.2	Toughness of the NPC gel	56
4.3.3	Strain hardening exponent of the NPC gel	66
4.4	Flat-ended model predictions.....	67
4.4.1	Blunt conical tip baculovirus	67
4.4.2	Blunt conical tip baculovirus – modified model.....	71
4.4.3	Sharp conical tip baculovirus.....	73
Chapter 5: Conclusion.....		75
5.1	Baculovirus nucleocapsid rides on the actin tail.....	75
5.2	Baculovirus entry into NPC	76
5.3	Concluding remarks and future work	77
Bibliography		80

List of Tables

Table 2-1 Different observations of actin propulsion studies and the corresponding modeling approaches.....	21
Table 2-2 Models for nucleocytoplasmic transport models.....	30
Table 3-1 Summary of the parameters of actin propulsion model.....	40
Table 4-1 Summary of the gel toughness and other properties of the <i>in vitro</i> hydrogels.....	56
Table 4-2 Toughness and shear modulus values for rubber, human skin and NPC gel.	65
Table 4-3 Summary of the parameters of the soft solid penetration model.....	67
Table 4-4 Punching force of the flat-ended model for different α values.....	67
Table 4-5 Force values for the case study of $\alpha=3$ and different toughness values	69
Table 4-6 Force values for the case study of $\alpha=4$ and different toughness values	70
Table 4-7 Force values for the case study of $\alpha=2$ and different toughness values	71
Table 4-8 Force values for the case study of $\alpha=3$ and different toughness values	72
Table 4-9 Force values for the sharp model with $\alpha=3$ and different toughness values	73
Table 4-10 The total punching force (pN) predicted by each model for $\alpha=3$ for different toughness values	74

List of Figures

Figure 2-1 Schematic diagrams of the structure of baculovirus occlusion bodies (OB) and occlusion-derived virion (ODV) along with budded virion (BV). Reprinted from [5] © 2013 by Au et al.....	6
Figure 2-2 SEM micrograph of the <i>listeria</i> riding on actin comet tail inside the host cell. reprinted from [13] (© 2008 Springer).....	10
Figure 2-3 Top: The schematic representation of the actin gel layer formed on the surface of the bacterium, which after the symmetry breaking process generates the comet tail. The elastic force F_1 is the propulsive force generated by actin polymerization and F_2 is the surface friction. Bottom: The force-velocity profile predicted by the macroscopic (continuous actin gel) model. Printed from [13] (© 2008 Springer).....	13
Figure 2-4 Schematic of the free-filament end model at rear of the bacterium (printed from [18] © Springer-Verlag 2008) and the predicted force-velocity relation (solid and dotted line) by the model which matched the experimental data (black points) (printed from [23] © 2003 by the Biophysical Society)......	16
Figure 2-5 Schematic of protein-associated model and the predicted force-velocity relationship by the model for different values of the mean filament spacing (printed from [26] © 2002 by the Biophysical Society).....	18
Figure 2-6 Diagram of the NPC Architecture. A cross-section of the NPC is shown with its ring scaffold, its cytoplasmic fibers, a putative meshwork of FG-domain filaments in its center, and the nuclear basket structure (printed from [49] © 2007 Elsevier Inc.).....	24

Figure 2-7 Schematics of the 3 different models on NPC structure: Right) The selective phase or the saturated hydrogel model, Middle) The virtual gating or polymer brush model, (printed from [50] © 2007 Elsevier Inc.). and Left) The hybrid Forest model. 29

Figure 3-1 Schematic of the TBR model proposed by Mogilner and Oster (2002) and the predicted force-velocity profile [23] © 2003 by the Biophysical Society. 33

Figure 3-2. The predicted force- velocity profile of the baculovirus riding on the actin comet tail. 42

Figure 4-1 Left) Schematic of the flat-ended punch penetrating into the soft solid. Compressed column of radius $b < R_b$ is shown in darker grey color. Right) Schematic of the infinitesimal layers of increasing radius in the tip of the Baculovirus. 46

Figure 4-2 Right) The punching pressure profile versus non-dimensionalized $J_{IC}/\mu R$ parameter; Left) The minimum crack opening versus non-dimensionalized $J_{IC}/\mu R$ parameter, for the flat-ended punch [64]. 47

Figure 4-3 Schematic of the flat-ended punch penetration into the soft solid. 48

Figure 4-4 Right) The punching pressure profile versus non-dimensionalized $J_{IC}/\mu R$ parameter; Left) The minimum crack opening versus non-dimensionalized $J_{IC}/\mu R$ parameter, for the sharp-ended punch [64]. 49

Figure 4-5 Electron micrographs of the baculovirus nucleocapsid, showing the morphology of the nucleocapsid with its two distinct ends; a blunt end and a conical end with a small protuberance. Scale bar is 50 nm (Printed from [3] © 2011 Elsevier Inc.). 50

Figure 4-6 The correlation between the gel concentration and elastic modulus (Blue line) and gel concentration and its toughness (red line), reprinted from [82] © 2015 American Chemical Society. 60

Figure 4-7 Number of the residues of the 3 main nups in the NPC central channel and number of FG-repeats per 100 residues [85]...... 62

Figure 4-8 a)3D simplified and non-exhaustive schematic diagram of nucleoporin localization within the metazoan NPC (printed from [86] © 2005 Elsevier Ltd) b) Model of the nuclear pore complex: The complex consists of an assembly of eight spokes attached to rings on the cytoplasmic and nuclear sides of the nuclear envelope [87] © Dr. G. R. Kantharaj..... 63

List of Abbreviations

AFM: atomic force microscopy

BR: brownian ratchet

BV: budded virion

EBR: elastic brownian ratchet

FG: phenylalanine-Glycine

NE: nuclear envelope

NES: nuclear export signal

NLS: nuclear localization signal

NPC: nuclear pore complex

NTR: nuclear transport receptor

OB: occlusion bodies

ODV: occlusion-derived virion

TBR: tethered brownian ratchet

SEM: scanning electron microscopy

WASP: wiskott-aldrich syndrome protein

Acknowledgements

I would like to offer my enduring gratitude to my supervisor, Professor James J. Feng, without whose support and help, I would not be able to finish this thesis. He taught me a lot of things, from critical thinking to how to be passionate on the research and stay motivated when I got disappointed with the research.

I would also like to appreciate all the helps from Mr. Brian Merchant, for all his help and courage during different parts of this project. With his valuable questions, I learned how to see things from different prospective. I also would like to acknowledge the envious level of patience and mentorship of Prof. Leah Edelstein-Keshet for her many valuable advices during my MASC studies. I would also express my deep gratitude for my committee members Dr. Nelly Panté and Dr. Alireza Nojeh. Special thanks to Dr. Nelly Panté who provided me with her endless guides and feedback on the different parts of this project. I have truly enjoyed our interactions during the last 2 years and my project would not have been possible without her assistance

I owe particular thanks to my sisters Ms. Fatemeh Navaee, Ms. Behshid Tavassolian, and my wonderful warm-hearted friends Ms. Parisa Sarmadi and Ms. Anupama Sharan and Mr. Brian Merchant and many others who had always supported and encouraged me in many ways. Special thanks to my parents and my younger brother, who have supported me throughout my years of education, and for providing me with your unconditional love.

Dedication

To my parents...

The reason for what I became today.

Thanks for great support and continuous love

And my loving brother...

Who always believes

Chapter 1: Introduction

1.1 Motivation and objectives of this thesis

In this MASC thesis, the Baculovirus entry to the nucleus of the host cell is studied using a mathematical model. This research includes 2 parts: cytoplasmic trafficking of the virus and nucleus entry. Both are inspired by recent experimental observations:

- Ohkawa *et al*, [1] showed that the nucleocapsids of the *Autographa California* multiple nucleopolyhydrovirus (AcMNPV) (which from now on is referred to as baculovirus) undergo the intracellular trafficking driven by actin polymerization. They observed that immediately after entering the host cell, the virus generates thick actin cables and starts exploring the cytoplasm and finding its way to the nucleus entrances (NPCs). Other microbe-host interaction studies also confirm the role of actin assembly and dynamics in pathogenesis [2]. Inspired by these observations, the first part of this study focuses on the actin polymerization mechanism and the propulsive force generated by actin filaments at the back of the nucleocapsid to push it forward.
- Au *et al*, [3] using electron microscopy discovered that the nucleocapsid of baculovirus (a 250-nm long rod like structure) crosses the nuclear pore complex (NPC) of the host cell and enters the nucleus intact. Using several experimental conditions, they visualized the intact nucleocapsid interacting with NPC cytoplasmic filaments. These observations suggest a large deformation inside the NPC leaving it in an open state that allows the large cargo to travel across. The objective of the second part of this project was to build a mechanical model to describe the mechanism of this translocation phenomenon. The nuclear import of the baculovirus nucleocapsid is a vital event in the

life cycle of this pathogen, so understanding its underlying mechanisms will contribute to the development of intervention and treatment, and to its potential application as a gene therapy vector.

The research described in this thesis evaluate the actin polymerization force for the rod-shape baculovirus trafficking inside the cytoplasm of the host. It will also attempt to validate the hypothesis of the mechanical entry of the virus through NPC. More specifically, the following questions are addressed in this research:

- 1) How much force is generated by actin polymerization at the rear of the baculovirus inside the host cell?
- 2) How much force will stall the actin-based movement of the baculovirus?
- 3) How much force is required for breaking through the NPC and whether the force from actin propulsion would be sufficient for it?

I have used simulation techniques, and mathematical equations in combination with mechanical engineering principles to describe the phenomenon mentioned above. The specific objectives of my master thesis were the following:

1.1.1 Characterization of actin propulsion for Baculovirus

The propulsion of the baculovirus nucleocapsids by the nucleated actin inside the cytoplasm of the host cell has been observed experimentally in different studies. Empirical findings suggest that cytoplasmic actin and the Arp2/3 complex on the surface of the nucleocapsid are two critical factors for intracellular trafficking and nuclear import of the viruses [1]. Since this actin polymerization and propulsive forces are a vital part of the baculovirus life cycle, many recent studies had focused on the role of actin polymerization, its underlying mechanisms and the actin-based motility of objects. Here in this study specifically we are trying

to shed light on the molecular basis of actin-based motility and mechanisms underlying the force generation. Using a mathematical model, we estimated the velocity of the virus being propelled by the actin comet tail, and the amount of external force required to stall its movement.

1.1.2 Elucidation of a potential role of phenylalanine-glycine (FG)-Nups in the nuclear import of the virus

The NPC seems to undergo large deformations and dynamic rearrangements to accommodate passage of the large nucleocapsids of baculovirus. This nuclear import process does not seem to involve the classical pathways with nuclear transport receptor (NTR) or nuclear localization signal (NLS). The FG-regions of the NPC nucleoporins (nups) is known to play an important role in the efficiency of baculovirus nuclear entry. However, a detailed understanding of the interaction of the virus with them, and the mechanism by which the virus opens the central channel and passes through NPC are missing. Here in this study we investigated the hypothesis of mechanical breakthrough by the virus and its interactions with FG-nups.

1.1.3 Evaluating the properties of the NPC central channel

Microscopic techniques have been widely applied to study intracellular organelles and to help correlating the structure and functionality of them at the sub-cellular level. Among all intracellular organelles, the nuclear pore complex the molecular mechanisms of nuclear translocation have remained elusive. The main difficulty in explaining these mechanisms is the lack of *in vivo* experimental data to test different hypotheses. Assuming that the central channel of NPC is filled with FG-repeat regions of the nups, several models have been presented to explain the nuclear import mechanism. A few experimental studies have suggested that whatever fills the central channel of the NPC must be very flexible and capable of large deformations in the form of retractions into the membrane-embedded scaffold ring of NPC [1, 4]. Dynamic

relocalization of the nucleoporins inside the NPC central channel as well as structural changes to the NPC cytoplasmic filaments are necessary to accommodate the intact nucleocapsid of baculovirus. Only in this case, NPC will be able to allow the passage of large cargo like baculovirus capsid.

1.1.4 Evaluating the mechanical entry hypothesis

The nuclear entry of baculovirus is proposed to be a unique receptor-independent mechanism which is not clearly understood. Therefore the dynamic flexibility of the NPC along with properties of the virus facilitating actin polymerization can potentially explain the experimental observations of the intact nucleocapsid passing through the NPC. Experimental finding shows that the NPC central channel is normally closed with the extended naturally unfolded FG-filaments [4]. However, central channel of NPC can undergo conformational deformation and open the pore if a large cargo is thrust it with sufficient force.

Chapter 2: Literature review

2.1 Baculovirus: The largest virus replicating in the nucleus of the host cell

2.1.1 Structure and life cycle

The baculovirus nucleocapsid is a rod-shaped, enveloped, double-stranded DNA virus that can replicate in the nucleus of the host cell. This insect-specific virus plays a major role in natural insect population control and can potentially be used as gene therapy vector to transduce mammalian cells. The first step toward these applications would be to understand the life cycle and structure of this virus and how it behaves inside the host cell and the mechanism by which it delivers its genome to the nucleus of the cell [5].

Baculovirus can be found in two infectious viral particle types: budded virion (BV) and occlusion-derived virion (ODV), both of which contain the baculovirus nucleocapsid. This nucleocapsid, has a rod-like structure with an apical cap end with a small protuberance and a blunt end (figure 2-1). Its size ranges from 250-300 nm in length and 30-60 in diameter [5] and encloses the circular, super-coiled dsDNA genome. The barrel of the nucleocapsid is mainly made of VP39 protein, with smaller amount of VP78/83 protein located at the blunt end of the rod which is known to be responsible for the actin nucleation [6].

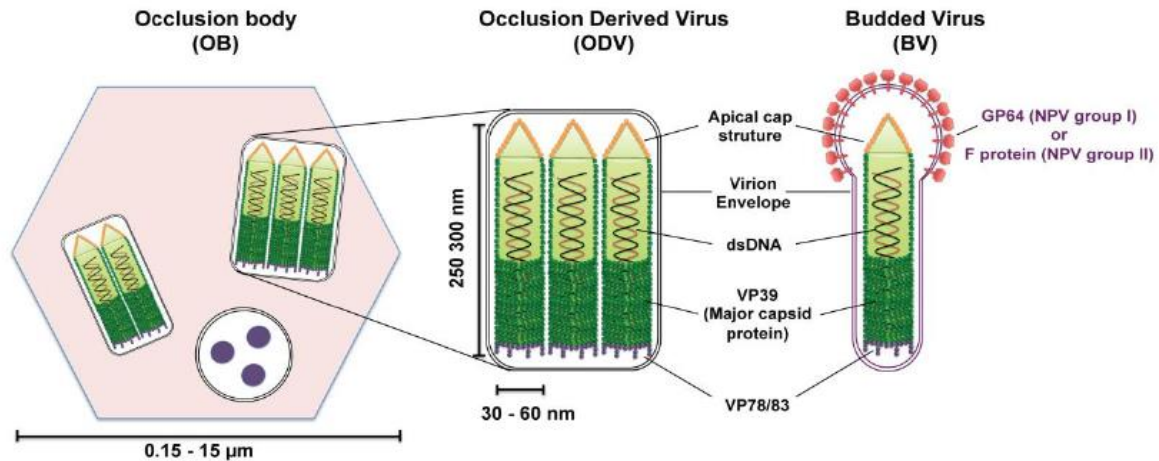


Figure 2-1 Schematic diagrams of the structure of baculovirus occlusion bodies (OB) and occlusion-derived virion (ODV) along with budded virion (BV). Reprinted from [5] © 2013 by Au et al.

The infection cycle of the virus starts with endocytosis. Soon after that, the endosomal membrane is fused with the viral envelope, which results in release of the nucleocapsid. The nucleocapsid is then transported to the nucleus by the actin polymerization. Upon entering the host nucleus the viral DNA is released into the nucleus and undergoes the replication process. The DNA replication is then followed by the transcription and nucleocapsid assembly. The nucleocapsid finally leaves the host nucleus acquiring an envelope from the nuclear bilayer. Reaching to the plasma membrane it will leave the cytoplasm and enter another infection cycle [3].

2.1.2 Baculovirus applications

BEV system has many attractive features as a potential gene therapy vector, including easy manipulation, ability to carry large and multiple DNA inserts, high titer production and purification [7], low toxicity and the capability to transduce mammalian cells. Baculovirus expression vectors (BEVs) were also used in induced pluripotent stem cell generation [8]. Their intrinsic capabilities for translocation inside the cytoplasm and passing through the nuclear envelope, can potentially enhance the efficiency of the gene delivery vectors [8].

Baculovirus also has potential applications in vaccination, cancer therapy, and drug screening. The recombinant baculovirus has been also used in vaccination proposes. This will provide an efficient gene delivery to the immune competent cells without severe toxicity. It is also capable of transducing stem cells, mediating a high-level transient expression of transgenes; present a unique advantage over routine chemical and physical transfection methods. Another application of baculovirus is in cancer gene therapy; where effective transduction and high-levels of transgene expression are required. Viral-based systems could be also implemented in assay development and drug screening applications. They have been routinely used for production of the recombinant proteins used in biochemical assays and structural chemistry experiments [8].

2.1.3 Intracellular trafficking of baculovirus

It has been shown that the baculovirus has an envelope containing glycoproteins, which are the essential components for cell binding and intracellular trafficking of the virus. A common way for viruses to be transported inside the cytoplasm of the host is to use the microtubules or actin filaments to reach to the nucleus surface. For baculovirus this transport is solely actin-based, meaning that once the nucleocapsid of the virus is in the cytoplasm of a cell, tick actin cables will be generated at the back of the virus and will push it toward the nucleus. These actin tails can be generated only if the virus has a certain surface protein. The blunt end of the baculovirus is covered by a layer of VP78/83 protein, a protein from Wiskott-Aldrich syndrome protein (WASP) family that promotes actin nucleation [5]. Therefore if the virus-infected cell is treated with actin polymerization suppressors or Arp2/3 inhibitors, the viral infection efficiency significantly drops, since the virus will not be able to get to the nucleus of the cell [5]. The detailed mechanism of actin-based motility and actin propulsion will be discussed later.

2.1.4 Nuclear envelope in viral infection

Entering the nucleus of the host cell, is one of the main stages in the viral life cycle of baculovirus. However, cellular membranes are the most important barrier they need to overcome. As mentioned earlier most of the viruses pass through the plasma membrane using endocytic pathways followed by the release of the nucleocapsid or the genome in the cytoplasm. The genetic material needs to reach the nucleus of the host in order to replicate. But the double-layer membrane of the nucleus is difficult to penetrate. For normal cellular and metabolic processes the transport occurs only via the NPCs. The macromolecules covering the NPCs prohibit the free flow of larger molecules and thus maintain the barrier between cytoplasmic and nucleus compartments. However, viruses have developed amazing ways of interacting with the NPC entering and exiting the host nucleus. They accomplish this task by one of several different ways, including making use of the nuclear pore complex and dissolving the integrity of the nuclear envelope [1]. In this research we will develop a mathematical model to study the mechanism by which the baculovirus enters the nucleus through NPC.

2.2 Actin polymerization

Actin is the most abundant protein in the cytoplasm of the cell, and polymerizes into long, thin and flexible fibers of 7 nm (in diameter), which later can be assembled into more complex structures like bundles and 3-dimensional networks and regulates a variety of cellular processes. Actin polymerization is a reversible process that plays a critical role in cell crawling, cell division and phagocytosis [9]. Polarity is the key component of the actin polymerization and tread-milling which is the dynamic process of monomer addition and subtraction at the two ends of the generated filament. In other words, actin monomers are constantly being polymerized in

one end of the bundle and depolymerized in the other end of the filament. Regulatory proteins called actin-binding proteins can stabilize the actin network by cross linking them to one another or can affect the treadmilling speed of the actin filaments. Some facilitate the elongation of the bundle by activating actin nucleation or enhancing polymerization, whereas others decelerate the filament elongation by increasing the monomer dissociation rate (depolymerization) or by capping the activated polymerizing sites [10].

Viruses and bacteria alike may utilize this actin-based motility machinery to infect the host cells. Study of the *Listeria* bacterial pathogen trafficking inside the host cell shows that they are capable of forming a tail of endogenous actin filaments which asymmetrically grows and produces a driving force to propel the pathogen (figure 2-2) [11]. Investigating this intracellular rocketing mechanism shows the presence of Arp2/3 protein family on the surface of these pathogens [11]. Evidences suggest that the initial and rate-limiting step in actin polymerization is actin nucleation which requires single monomers interacting correctly. The Arp2/3 proteins is capable of forming stable actin dimers which can later act as a cryptic nucleus for filament formation [11]. By attaching to the side of an existing filament they can also form a new branch [12].

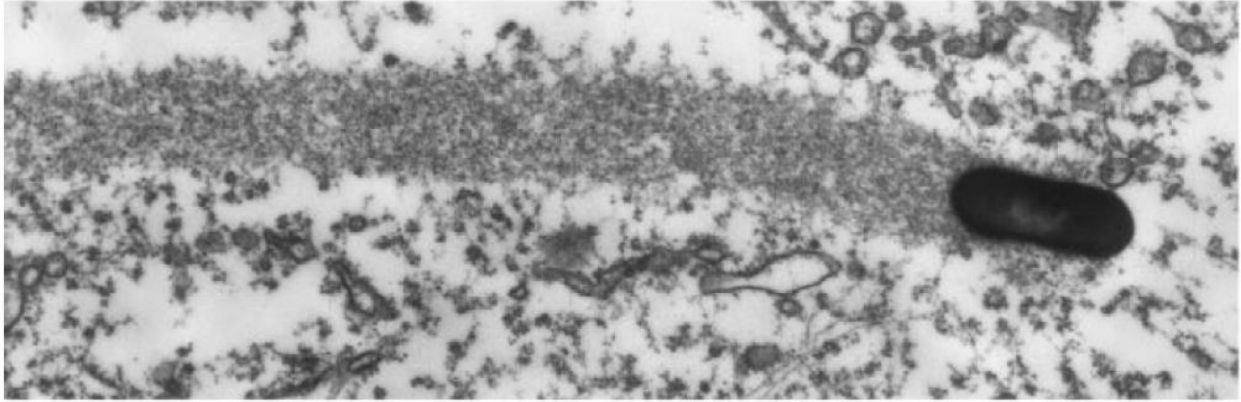


Figure 2-2 SEM micrograph of the *listeria* riding on actin comet tail inside the host cell. reprinted from [13] (© 2008 Springer).

Several studies on deformable soft particles like vesicles and oil droplets have been used to estimate the magnitude of the normal force generated by actin polymerization. For example, Upadhyaya et al. [14] and Giardini et al. [15] both found that initially spherical ActA coated vesicles evolved to teardrop shapes during actin-based propulsion in cell extracts. Their model results indicated that the net actin polymerization force exerted orthogonal to the surface of the droplet is greatest on the vesicle sides and minimal at the vesicle rear. In fact, they found that the net forces in the rear of the vesicle are oriented opposite the direction of motion, suggesting a spatial partitioning of pushing and retarding forces. These results directly demonstrate that forces generated by actin comet tails are largely compressive rather than simply propulsive [15]. Other particle-based systems for studying actin propulsion were not used to measure the magnitude, direction, and distribution of the forces generated at the actin–membrane interface. Lipid-vesicle experiments provide direct visual demonstration of the distribution of actin forces on a moving load represented by the changes in vesicle shape. Based on these results, actin exerts both retractile and propulsive forces depending on the local membrane curvature. It has been said that some of the actin filaments may be tethered to the vesicle surface, whereas others are free to

polymerize. In response to the membrane stretching due to deformation, the tethered filaments exert a tensile stress on the membrane surface [14]. In a study of actin-propelled lipid vesicles in cell extracts, the vesicles were also found to be pushed by the filaments attached to their sides, and being pulled by the filaments attached to their tails [16].

Beside those experimental researches, some other studies have been focused on the detailed mechanism of actin propulsion and evaluation of the generated forces. Aiming to quantify the actin tread-milling, initial attempts using mathematical modeling was made in 1993 [17] to understand the nature and magnitude of the actin polymerization force. The findings of these early studies along with the experimental measurements of the actin polymerization and disassembly rate are key inputs in the theoretical modeling of actin-based motility. A combination of chemical kinetics, transport phenomenon and physical forces along with polymer science has been used to formulate the problem and its biological and mechanochemical kinetics [18].

One of the advantages of studying this problem in the context of mathematical and theoretical models is the fact that one can introduce new ideas, evaluate non-obvious hypotheses and provide mechanistic interpretations of the experimental results. Existing literature on actin polymerization models can be divided into 3 different categories, each focusing on one of the key aspects of the process. Macroscopic continuum mechanic models consider the actin comet tail as a continuous gel which is elongating by polymerization at the barbed end and provides the propulsive force. Another group of the models are mainly focused the molecular mechanisms by which the energy is generated and released in the form of mechanical work to push the object forward. A third group of models, proposed very recently, are hybrid models considering the

concepts and principles from both continuum mechanics and molecular interactions in actin propulsion.

2.2.1 Macroscopic approach

The first approach is macroscopic continuum modeling of actin comet tail at the rear of the *Listeria* [13]. They have considered the actin comet tail as an elastic gel growing on the surface of the object, as a result of actin polymerization process. For a spherical bead coated with ActA in a cell extract or in a reconstituted extract containing all relevant proteins and energy sources, it has been shown that the kinetic rates of actin polymerization and depolymerization depend on tension. When both rates take on the same value, a steady state is reached. The principal idea behind this gel extension model is a positive feedback concept that makes the gel growing on the rear side and getting thinner on the front surface of the object. For example, elevated depolymerization rates due to the higher tensile stress on the thinner parts of the gel on the surface of the object will further decrease its thickness and increase instability of the gel. Upon a symmetry breaking process, a tail of actin gel is formed at the rear of the object which is capable of pushing forward and move the object around [13] (figure 2-3).

Some studies indicate that the actin propulsive force at the rear of the bacterium is decreasing by velocity. For example, in 2004 Marcy et al [19]. had directly measured the actin-based propulsive force, using a micromanipulation experiment. Then using a mesoscopic elastic analysis, initially proposed by Gerbal et al. [20], and simplifying formulation based on Flyvbjerg's dimensional analysis [21], they found a shallow force–velocity curve and predicted that forces of the order of nanonewtons can potentially slow down *Listeria* movement [19].

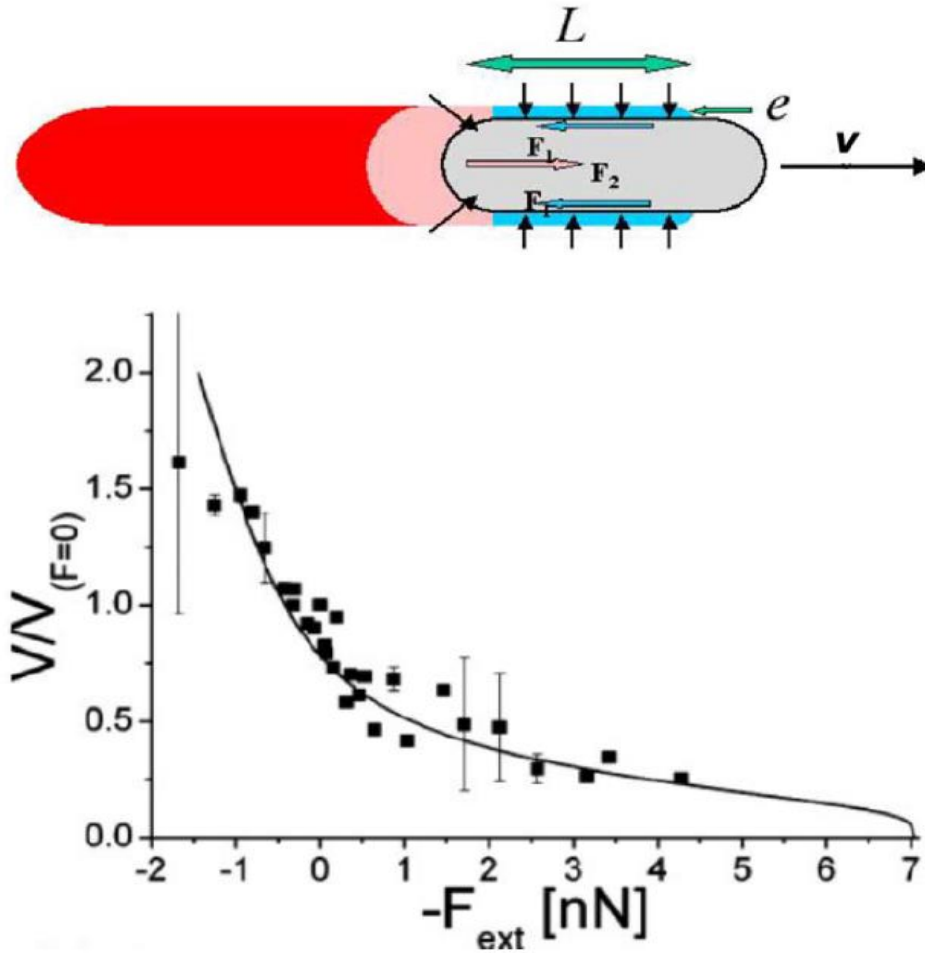


Figure 2-3 Top: The schematic representation of the actin gel layer formed on the surface of the bacterium, which after the symmetry breaking process generates the comet tail. The elastic force F_1 is the propulsive force generated by actin polymerization and F_2 is the surface friction. Bottom: The force-velocity profile predicted by the macroscopic (continuous actin gel) model. Printed from [13] (© 2008 Springer).

2.2.2 Microscopic approach

In order to understand the molecular mechanisms underlying actin polymerizations, some models had implemented a more detailed approach to explain the actin force generation. In the microscopic approach, the molecular mechanisms driving actin polymerization explain how the chemical energy released upon actin polymerization is converted into a pushing force on a

surface. Several models have been proposed based on this approach and have attempted to explain puzzling properties of actin-based motility, including persistent attachment of the network to the membrane during propulsion and the interesting trajectories of propelled particles. In general, these models are classified into 2 sub-groups: free filament end models, and protein-associated models.

2.2.2.1 Free filament-end models

The microscopic model first introduced in 1993 by Peskin et al. sought to present the exact mechanism of actin force generation and suggested the Brownian Ratchet model [17]. According to this model thermal fluctuations of the bacterium would provide a required gap between the rigid actin polymer and the rear surface, so that one single G-actin monomer could intercalate into the gap and bind to previous filaments. This way the fluctuation is moved one step forward. Considering the propulsion simply as Brownian diffusion rendered unidirectional by the polymerization of the actin tail (the diffusion-based movement of the object), these models predict a certain profile for force-dependent velocity of the object (figure 2-4).

Besides, observing actin filaments being more often tethered to the surface of the object, in 1996 Mogilner and Oster modified the BR model and suggested the Elastic BR model where each individual actin filament is thermally fluctuating (bending undulation) and these fluctuations create the required gap for monomer diffusion and polymerization [22]. The mean field theory they have used is that they assumed independent filaments growing with the same speed, subject to the same load force, and exerting the same undulation force on the load. Afterwards, in trying to find an answer for how these filament can bend and generate the gap while they are attached to the bacterium surface, the same group had reached the idea of transient attachment of actin filaments to the surface [23]. Therefore the idea of the Tethered BR model is

presented by the same group in which 2 separate groups of filaments exist: one attached to the bacterium surface and one dissociated and fluctuating. This model can also predict the moving velocity of the object and its correlation with applied external force. This approach had also proposed a size-dependency of propulsion velocity which obviously contradicts the diffusion-based movement proposed by Peskin et al. Based on these predictions the smaller the object is, the slower it moves forward by actin propulsion. This observation is justified by the fewer number of actin filaments attached to the surface of the smaller objects [18].

This idea is also confirmed by experiments done by Cameron et al. who using electron microscopy images tried to visualize the individual actin filament attached to the surface of polystyren microparticles [24]. This experiment also validated the hypothesis of non-permanent filament-bead interactions and that they are undergoing cycles of association and dissociation. However, Wiesner et al. in 2003 reported that movement of the Act-A coated beads was not slowed down by increasing the diameter of the beads (0.2 to 3 μm) nor by increasing the viscosity of the medium by 10^5 -fold [25]. Experimental results of Marcy et al. suggest a force-velocity profile consistent with that of Mogilner's model predictions [19]. They proposed that within a microscopic model, the relation is essentially biphasic with a rapid decay for small forces and a smooth one for higher forces. They found that the relation is linear for pulling forces and decays more weakly for pushing forces. This behavior is explained by using a dimensional elastic analysis [19].

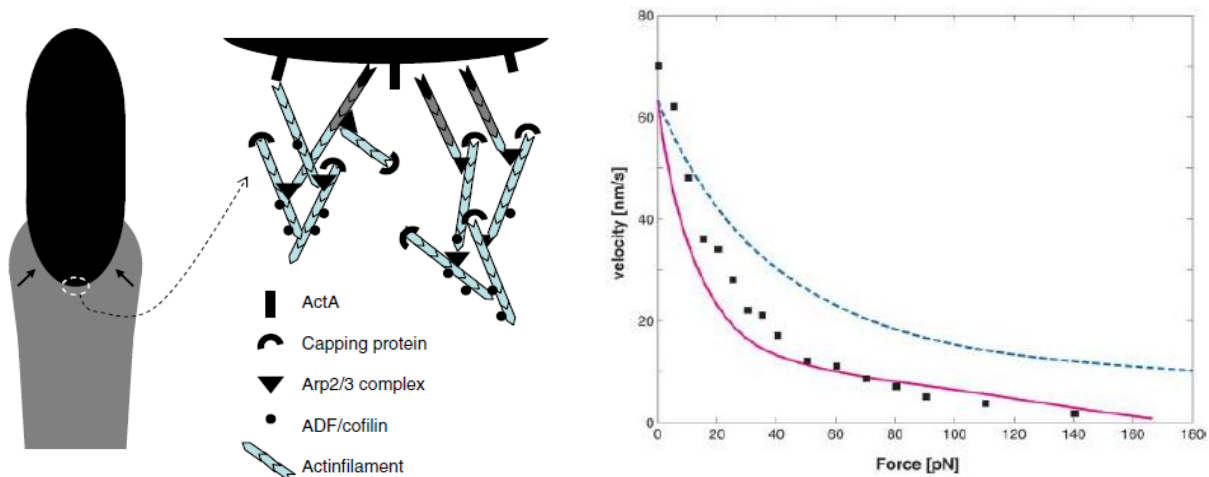


Figure 2-4 Schematic of the free-filament end model at rear of the bacterium (printed from [18] © Springer-Verlag 2008) and the predicted force-velocity relation (solid and dotted line) by the model which matched the experimental data (black points) (printed from [23] © 2003 by the Biophysical Society).

2.2.2.2 Protein-associated models

Another group of models for estimating the actin propulsive force in the microscopic approach are based on the role of the molecular motors. In 2002 Dickinson et al [26], claimed that the rapidly elongating cytoskeletal filaments persistently tethered at their polymerizing ends to propelled objects cannot be explained by force-generation models that require free (i.e., untethered) filament ends to fluctuate away from the surface for new monomer addition. In contrast, filament end-tracking proteins that advance on filament ends can facilitate rapid elongation and substantial force generation by persistently tethered filaments (figure 2-5) [27]. Their prediction of force-insensitive filament elongation and elongation of attached filaments at small to moderate compressive or tensile loads is a key difference between the Brownian ratchet models (which predict an exponential decrease of elongation rate versus load). This predicted force-elongation rate dependence of end-tracking motors qualitatively agrees with recent AFM-based experiment on force velocity profile of *in vitro* actin polymerization [28]. Parekh et al.

obtained force–velocity (Fv) measurements of growing actin networks *in vitro* until network elongation ceased at the stall force. They found that the growth velocity of a branched actin network against increasing forces is load-independent over a wide range of forces before a convex decline to stall.

Carlsson [29, 30] found a similar relation for the dendritic nucleation scheme but with essentially no decrease in velocity in relation with force for the autocatalytic filament branching scheme. Based on their observations, the effect on the growth rate is quite small, which is surprising given that single filaments obey an exponential decay law. As the force increases, the force per filament in fact remains rather constant as the number of filaments in contact with the obstacle increases. In other words, a self-regulating effect is controlling the velocity, which implies the force dependence of the network density. The density is roughly linear as a function of the force. They believe that this effect is due to the fact that as the force increases, the leading filaments will push into the obstacle (or bend, actually), allowing other filaments to remain in contact with the obstacle and thus to keep branching and growing. As mentioned earlier, in 2003, Wiesner et al. had also shown that the medium viscosity does not affect the velocity [25], which further emphasizes the force-independent nature of propulsion velocity.

Despite these experimental evidences on the force-independent velocity profile, it is worth mentioning that the protein associated model does not provide any model verification using experimental data. In other words, comparing the force ranges and velocity changes in the experimental studies mentioned above and the ranges suggested in figure 2-5, none of the experimentations matches exactly those model predictions. On a side note, we were not able to reproduce the predictions of protein associated model, and we suspect an error in the

computations of [27]. Therefore for this study, the free filament-end model has been integrated for the case of baculovirus nucleocapsid.

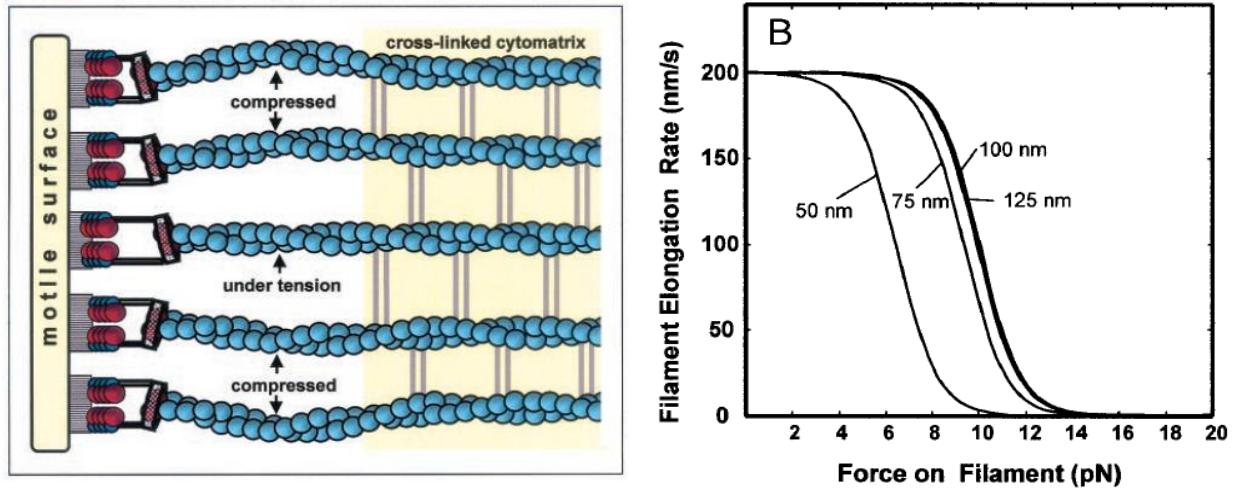


Figure 2-5 Schematic of protein-associated model and the predicted force-velocity relationship by the model for different values of the mean filament spacing (printed from [26] © 2002 by the Biophysical Society).

Using an energy-minimizing function Mueller et al. in 2014 have simulated the structure of actin comet tails as well as the tracks adopted by baculovirus in infected cells *in vivo* [31]. They demonstrated that propulsion is based on the assembly of a fishbone-like array of actin filaments organized in subsets linked by branch junctions, with an average of four filaments pushing the virus at any one time. Their simulation results ruled out gel squeezing models of propulsion and support those in which actin filaments are continuously tethered during branch nucleation and polymerization. Although they proposed that both microscopic polymerization ratchets and macroscopic stresses of the deformable actin network affect the force and movement generation, they have focused much more on the structure of the comet tail rather than the nature of the forces and speed of object movement [31].

2.2.3 Mesoscopic approach

The third approach for studying the force generated by actin polymerization is the so-called “mesoscopic model” [32]. In this new approach, Zhu and Mogilner had combined the concepts of the two theoretical models dominating current understanding of actin-based propulsion: microscopic polymerization ratchet model and macroscopic elastic propulsion model. They examined - both experimentally and computationally - the 2D movement of ellipsoidal beads propelled by actin tails and showed that neither of the two models can explain the observed bistability of the orientation of the beads. Therefore, to explain the data, they developed a 2D hybrid mesoscopic model by reconciling these two models. Specifically, they considered the nucleation, elongation, attachment, detachment and capping of each individual actin filament, and embedded these into the boundary of a viscoelastic network representing the macroscopic actin gel. Their simulation results fit the experimental data. Based on this hybrid model, they observed both force-velocity relations for different object morphologies: Those ranged from concave-down (velocity of protrusion being insensitive to the load up to a threshold and plunging to a stall at a critical opposing force, as of Dickinson’s results and *Parekh*’s experimental data) to concave-up (more or less exponential decrease of the velocity with the growing load which is consistent with Mogilner’s predictions and *Marcy*’s observations) relations [32].

Another mesoscopic model, proposed in 2010 by Schreiber et al. [33] is very different from this one. Considering microscopic models of propulsion as boundary conditions for the viscoelastic actin gels, this stochastic simulation is based on the key fundamental properties of actin polymerization, such as growth, shrinkage, capping, branching, and nucleation, and also includes contributions from the creation and breaking of adhesive contacts with the substrate

together with excluded volume effects related to filament packing. This simulation generated a force–velocity relationship that resembled closely that concave-down relations observed experimentally [33]. In 2009, Lee and Liu also reported numerical simulation results for the force-velocity relation for actin-polymerization-driven motility. Using Brownian dynamics to solve a physically consistent formulation of the dendritic nucleation model with semiflexible filaments that self-assemble and push a disk, they found that at small loads, the disk speed is independent of load, whereas at high loads, the speed decreases and vanishes at a characteristic stall pressure [34]. The prediction that the velocity of a moving cell indeed goes to zero for some finite stall force F_{stall} contrasts with the purely Brownian ratchet model that predicts an asymptotic approach to zero velocity. The difference probably derives from the fact that the force–velocity relation in this model contains important contributions from excluded volume-related swelling and adhesion to the substrate.

2.2.4 Concluding remarks on actin-propulsion models

In summary, among many different models proposed for actin propulsion, perhaps the tethered brownian ratchet (TBR) approach presented by Mogilner and Oster is the most comprehensive microscopic model. However, some other aspects can also be considered to complement their model. For instance, they had considered a single independent filament and steady state association/dissociation of the attached/working filaments. The effect of actin (autocatalytic) branching or filaments non-perpendicular to the surface which may not be contributing to the force, can also add value to the results.

Table 2-1 Different observations of actin propulsion studies and the corresponding modeling approaches¹

F-v profile	Study	Object geometry	Stall force	F-v profiles
Macroscopic approach	Prost (2008) [13]	Sphere	<10 nN	
Microscopic approach free-filament end model	Marcy (2004) [19]	Sphere	4.3nN for a 2μm bead	
	McGrath (2003) [35]	Listeria (ellipsoid)	~0.2nN	
Microscopic approach Protein-associated model	*Wiesner (2003) [25]	sphere	orders of nN for 2μm bead	
	Parekh (2005) [28]	flat disk	~300nN	
	Heinemann (2011) [36]	Flat (lamellipodium)	2.9nN	
	Prass (2006) [37]	Flat (lamellipodium)	1.18nN	
	Zimmermann (2012) [38]	Flat (lamellipodium)	<1nN	

¹ There might be some other molecular dynamic simulation studies and atomistic descriptions of the actin polymerization process; however, they are not relevant to the purpose of this study and estimation of the generated propulsive force and therefore those cases are not reviewed in this thesis.

² © 2008 Springer

³ © 2003 Elsevier Science Ltd.

⁴ © 2005 Nature Publishing Group

F-v profile	Study	Object geometry	Stall force	F-v profiles
Mesoscopic approach	Zhu (2012) [32]	Flat disk	80 nN	
Mesoscopic approach	Zhu (2012) [32]	Sphere	80 nN	

* In this research, they only investigated different external forces and showed that the velocity remains constant. It does not go further to reach the stall force and stop the object movement completely. (These results might not be considered as concave down profile; because what this study shows is just a force independent region (in range of 0.01-100pN of force load) where the motile velocity is not affected by external force).

Mogilner's model describes a mechanistic description at the molecular level but is inappropriate for the mesoscopic behavior of the bacterium, because it does not consider the interactions between the filaments. Potential generalizations of TBR model may include the idea that the tail behaves like a mechanical feedback system, keeping the speed of the bacterium fairly constant over a large range of force opposing its motion. There are experimental observations supporting such behavior. Table 2-1 summarizes the actin motility experimental results along with the theoretical predictions of the various models.

⁵. © 2012 Zhu, Mogilner.

⁶. © 2012 Zhu, Mogilner.

2.3 Nuclear pore complex

The nucleus of the cell being its main genetic information container is perhaps the most important organelle inside the cell. It is well protected by a double layer membrane called the nuclear envelope (NE). While providing this protective isolation for nucleus, this envelope also serves as a way for the nucleus to communicate with the rest of the cell. This communication is done through a set of pores in the envelope covered by numerous proteins responsible for regulating the exchange of materials into and out of the nucleus. These structures, called the NPC, are the only transport pathways into and out of the nucleus and are highly active and capable of transporting several hundreds of molecules per second with a certain level of specificity and selectivity [39, 40].

Callan and Tomlin had first observed organized annular structures (3-15 per μm^2) piercing the NE in 1950 [41]. After this initial observation, these macromolecular structures having eight-fold rotational symmetry embedded at fusion points of the NE have been studied more. Electron microscopy images of NPC show a complex symmetric cylinder with highly complicated evolutionary origin. NPC is composed of 3 rings: a central spoke ring sandwiched between the nuclear and cytoplasmic rings [41]. On the cytoplasmic ring, there are 8 cytoplasmic filaments responsible for transportation into the nucleus, capping the central framework measuring about 50 nm long [42, 43]. On the nuclear ring, the 8 nucleoplasmic filaments assemble to a basket-like structure for exporting cargos out of the nucleus with around ~100 nm length [44, 45]. The NPC central channel, embedded inside the nuclear envelope, is a structure made out of the natively unfolded and flexible proteins mounted on the central spoke ring, and measures approximately 40-75 nm in diameter and around 40-90 nm in length [46, 47].

Therefore the NPC is quite a large assembly spanning over 200 nm length and around 80 nm in diameter [47]; it can have a total molecular mass of 60-112 MDa (figure 2-6) [48].

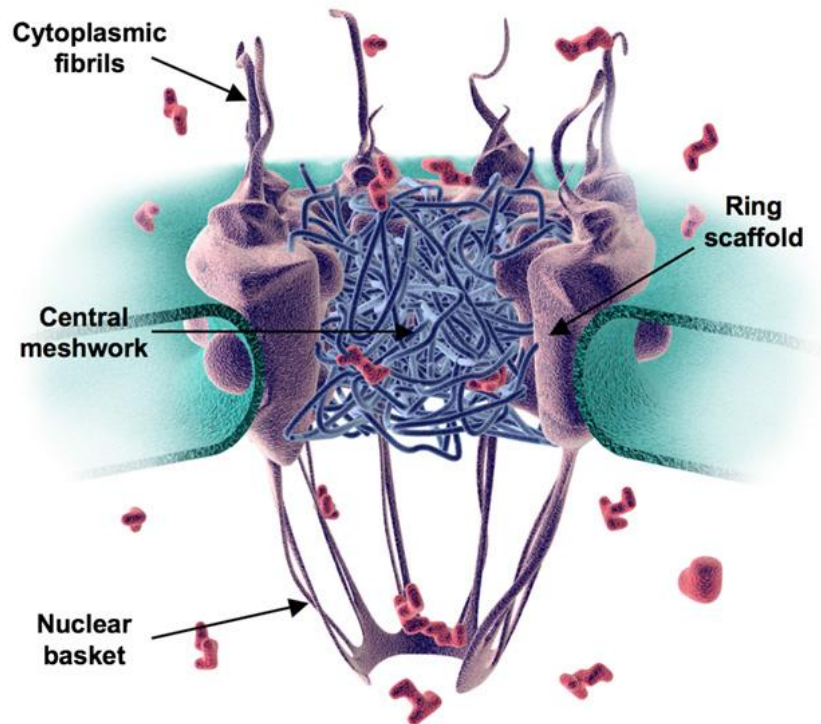


Figure 2-6 Diagram of the NPC Architecture. A cross-section of the NPC is shown with its ring scaffold, its cytoplasmic fibers, a putative meshwork of FG-domain filaments in its center, and the nuclear basket structure (printed from [49] © 2007 Elsevier Inc.).

There are 30 unique proteins in these 3 rings of NPC which are called nucleoporins (Nups) and make a stable dynamic assembly acting as a structural scaffold in central parts and also providing regulatory functions at the periphery. The nups in the central channel are responsible for the molecular exchange between nucleus and cytoplasm and allow the passage of any cargo through 2 main mechanisms determined by the molecular size of the cargo: passive diffusion for molecules smaller than 40 kDa and facilitated translocation mainly due to the hydrophobic-hydrophobic interactions of the nuclear transport receptors (NTRs) and the

phenylalanine-glycine (FG)-rich repeats of the nups in the central channel [50]. These FG-nups contain multiple small hydrophobic phenylalanine-glycine repeats and do not have any secondary structure so are free to diffusively writhe around the attachment site [51].

2.3.1 Mechanism of transport through the NPC

To understand the transport mechanism of NPC, one needs to study the operation of FG-nups translocation machinery. The structural nups in the central channel of NPC, are responsible for its shape and strength and also help maintaining the integrity of the NE. These nups representing almost half of the mass of the whole NPC, are classified as inner rings and outer rings and form a scaffold like structure through which the transport occurs. This scaffold serves both as a barrier with defined permeability and a facilitator for translocation of the selected molecules. Both of these roles rely on the current positioning of the critical nups. These nups create a dense meshwork and set an entropic barrier to macromolecules; however, cargos that bind to NTR or nuclear localization signal (NLS) can overcome this barrier [51].

Each cargo needs a specific signaling sequence to help translocate them into or out of the nucleus. NLS helps trafficking of a cargo into the nucleus and nuclear export signal (NES) targets the cargo going out of the nucleus. Besides these 2 main signaling amino acids, specialized proteins called Karyopherins (NTR that binds to NLS or NES) are also responsible for efficient transport of cargos. They recognize their cargo in 2 different ways: direct binding or binding via an adaptor protein. The most important concept in all these different trafficking modes is the dual functionality of the FG-nups in the central channel of NPC. They establish a diffusion barrier and at the same time an active transport pathway through the NPC. The basic principle of cargo transportation in active transport pathway is based on the fact that all the

NTRs have some low-affinity binding sites that can interact with thousands of FG-nups in the NPC channel [51].

2.3.2 Models on NPC structure and functionality

Despite enormous efforts for understanding this gating mechanism in NPC, the exact details of the process are still unknown. Several models have been proposed to explain the mechanism of cargo transport through NPC. The 2 main mechanistic models are the “virtual gating or the polymer brush” model which relies on a central channel formed by natively unfolded FG-nups; and the “selective phase or hydrogel” model which considers a uniform gel inside the central channel [5].

In the polymer brush model the translocation is mainly associated with rapid diffusion driven movements of the unfolded domains of FG-nups. An NTR would bind to the FG-repeats and passes through NPC, whereas a cargo not binding to NTR would be excluded from the NPC vicinity [52, 53]. However, the hydrogel model is mainly based on the cross-linked structure of FG repeats which is proposed to make a dense gel. NTR binding the FG repeats are able to dissolve these crosslinks and open up the gate, whereas other macromolecules can not go through [54, 55]. A third model also exists which considers coexistence of both structures with a meshwork-like gel at the periphery and the flexible unfolded proteins in the middle of the channel. Patel et al, studying the *in vitro* interaction of specific subset of FG-nups proposed a unified model of NPC architecture featuring two types of gates, one operating as a selective phase in the center and the other operating as a virtual gate at the periphery [49]. Results from a recent research confirms the coexistence of a viscous self-regulated central channel for diffusion of small/medium-sized molecules surrounded by distinct pathways accommodating NTR transportation [48].

2.3.2.1 Polymer Brush or Virtual Gating model

The virtual gating model assumes an entropic barrier in the NPC. In order for a molecule to pass through this barrier there is an activation energy required. This entropic barrier vanishes upon binding of transport receptors to non-interacting hydrophobic FG repeats of NPC. If a cargo is not bound to a transport receptor, the barrier becomes formidable and therefore only molecules of size up to around 30 nm can enter it. Larger molecules are stopped by the dense FG-nup gate. In this model, the central channel potentially allows anything less than 40 kDa to passively diffuse, but its specific dimensions and operating mechanism is yet to be explored [52]. The polymer brush model is an extension of the virtual gating model, and suggests that access for large molecules into the NPC is granted only if they can interact with individual protein. This means that FG nups are required to be flexible and capable of bending in presence of the receptors, so that the channel collapses and draws those molecules inside. With this kind of transient interaction between cargo complex and the FG filaments, larger molecules up to 100 nm could also penetrate the NPC. Small molecules would still passively diffuse into the NPC [53]. The oily spaghetti model also belongs to this group of models and it proposes an open pore of 10 nm in the central part surrounded by a layer of long hydrophobic FG repeats (spaghetti-like filaments) of 7 nm thickness which can be pushed aside by cargo complex and opened wider. The size of the molecule capable of passing through NPC in this model ranges from 9 nm with higher probability for particles smaller than 5 nm to ribosomal proteins [48].

2.3.2.2 Saturated Hydrogel or Selective Phase model

On the other hand, the selective phase or the hydrogel model suggests a meshwork with gel-like properties being formed in NPC by the FG-nups which makes a mechanical restriction for large cargos. In this model, the transport receptor cargo complex is assumed to randomly

move inside the meshwork and its transient interactions with FG repeats would allow it to dissolve in the NPC structure. The mesh size would determine an upper limit for the size of large molecules to passively diffuse through the structure along with randomly distributed holes of 2.6 nm throughout the gel which dramatically restricts the free passive diffusion. Transport complexes have transient multivalent interactions with FG-clusters, and are able to open the mesh and dissolve the meshwork across NPC. Therefore, the upper limit for the size of molecules to be transported by a cargo is 45 nm. Clearly the main difference between this model and the previous one is the separation of transport pathways for passive and facilitated transport in this model, without considering an existing collapsible central channel [54-57].

2.3.2.3 Hybrid or Forest model

In addition, based on some recent studies on the hydrodynamic properties of the FG regions, the selective permeability barrier consists of 2 different types of FG nups: collapsed FG nups (“shrubs”) and extended or relaxed FG nups (“trees”). In this model, so-called forest or hybrid model, there is a zone of passive diffusion for small molecules separated from a zone of facilitated translocation for cargo complexes. The first one forms an axial tunnel in the center and the second one locates in the periphery of NPC. The low charge FG nups can collapse and form a globular coil conformation (shrubs) which makes a thin hydrogel along the inner wall surface of the pore, while the highly charged ones stay in a highly dynamic highly coiled conformations and make the trees with an open central channel. This model assumes that larger cargos bound to the receptors will be handled through this central tunnel which can rapid deform to adapt molecules less than 36 nm in diameter. Smaller molecules would more likely use the peripheral zone between the exterior surface of the transporter structure and the inner wall surface of the conduit, where there are more extended and relaxed coils. Clearly this model

having the possibility of the passive diffusion occurring in both of the zone through multiple channels, is more sophisticated than the others [49, 58]. Recently, Goryaynov et al, [48] investigated the diffusion of intermediate sized cargo molecules through the central axial tube of NP. Their findings strongly support the idea of having 2 distinct zones in the NPC. Based on these results they confirmed the existence of a viscous central axial channel accommodating the diffusion of small (<20 kDa) and medium-sized (20-40 kDa) molecules. As opposed to existence of randomly distributed channels in the NPC like the selective phase/hydrogel model, this model proposes a structure more consistent with oily spaghetti and brush models; where smallest molecules can penetrate deeper in to the channel whereas the bigger ones will be kept in the more compact area by the protruding nups. Facilitated transport are done more through the peripheral zone and passive diffusion as mainly through the central channel [48]. Figure 2-7 shows the schematics of these three structural models of NPC. Table 2-2 summarizes the main features of all these models with the cut-off sizes for molecular translocation through NPC.

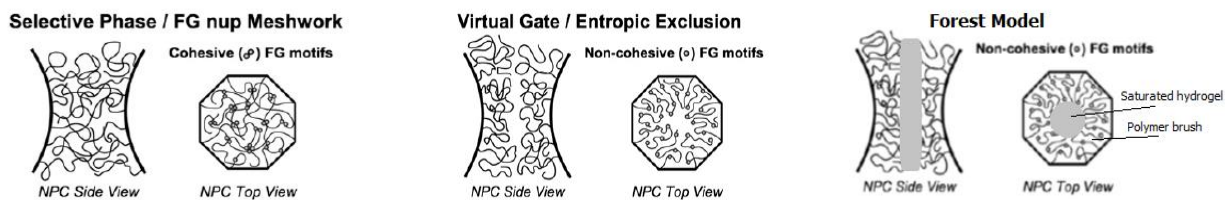


Figure 2-7 Schematics of the 3 different models on NPC structure: Right) The selective phase or the saturated hydrogel model, Middle) The virtual gating or polymer brush model, (printed from [50] © 2007 Elsevier Inc.), and Left) The hybrid Forest model.

Table 2-2 Models for nucleocytoplasmic transport models

NPC model	FG-nup structure	Passive diffusion	cut-off size	Facilitated transport	cut-off size	reference
Virtual gating	Non-interacting hydrophobic FG nups making a rigid gate on the internal wall of the ring	An entropic barrier formed by the dense FG-nups, constraining passive diffusion	Up to 40 kDa for neutral molecules	Several binding sites for transport receptors at both ends of NPC	Up to 30 nm in diameter	[59]
Polymer Brush	Reversibly collapsing FG nups upon interaction with receptor-cargo complex	Long filaments anchored on the ring side and extending to the pore milieu	Up to 40 kDa for neutral molecules	Temporary collapse of the FG nups activated by transport receptor	Large cargos up to 40 nm	[53]
Oily spaghetti	Hydrophobic randomly oriented FG nups, weak and transient binding of carrier proteins, with higher affinity outside and lower inside for easier transport of large cargos	Extended filaments in the pore like loose oily spaghetti	Channel of 10 nm	Random diffusion of the transport receptor between different binding sites	Up to 26nm in diameter	[52]
Selective phase/hydrogel	Interaction of Phe residues of the saturated FG repeats makes a dense sieve like gel	Several randomly distributed small holes	2.6nm in diameter	Receptor-cargo complex dissolves into the highly hydrophobic gel by disengaging the interrepeat contacts	45 nm in diameter or 530 kDa	[60]
Forest model	Negatively and positively charged domains in FG nups with globular conformation on the tip or extended coils, respectively form 2 distinct zones in NPC	Through both zones formed by the extended coils stuck together at their tips by globular conformations and collapsed coils	5-6 nm	Mediated by interaction with the extended coils of FG filaments. stalk zone on the periphery is used for the smaller cargos and the central zone is used for larger cargo complexes	36 nm	[48, 58]

All these hypothetical models try to establish a precise prediction of NPC features. All these features are extremely challenging to test *in vivo* due to the high variety of the methods and complex redundant structure of the FG-nups. Although these models assume different mechanisms for nucleocytoplasmic transport, they have the same range of cargo sizes for both diffusion and facilitated transport. So a more accurate estimation of the architecture and transport limitations of the structure is yet to be established. In order to find the right model the ideal case would be studying the NPC under physiological conditions in the living cell with a completely non-invasive technique.

Chapter 3: Actin-based locomotion of the Baculovirus

As mentioned in Chapter 1, several experimental and theoretical studies have focused on understanding the nature of the actin generated force and the force-velocity relationship of the motile surface, and develop a force-velocity profile for both *Listeria* and Act-A coated particles. In this research the actin locomotion of the baculovirus is studied with a microscopic approach. We adopt the elastic ratchet model presented by Mogilner and Oster for evaluating the force generated by actin polymerization [23]. Acknowledging the need for further experiments to distinguish the two microscopic approaches available, Mogilner and Oster modified the original elastic Brownian ratchet model to account for transient binding of the actin filaments to the object. They showed the only protein necessary for forming actin tails is ActA which nucleates nascent actin filaments and initiates actin propulsion.

Mogilner and Oster's motivation was experimental evidences showing that the actin tail is attached to the surface of the pathogen during propulsion. This observation contradicts other EBR models which rely on the gap between the actin filaments and the surface for monomer addition. The key assumption in Mogilner and Oster's model is that the attached filaments are under tension and resist the forward movement of the object, whereas the detached filaments are under compression and thus grow and push the object forward. These assumptions successfully explain the nature of actin polymerization and steady state propulsion.

3.1 Model set up

Several experiments focusing on the nature of the propulsive force reported a correlation between the density of the protein coating the surface of the object, its size and its velocity. These observations along with others regarding filaments length and architecture define the

model parameters. If the model predicts the observed experimental behavior one can claim that the model is essentially correct, even though there might be numerous unknown factors and parameters [23]. In their model, Mogilner and Oster [23], formulate a two-compartment model consisting of tethered filaments and dissociated ones with the latter being responsible for generating the protrusive force and both being anchored to surrounding cytoskeleton in their distal parts. The model consists of 3 sets of equations: 1) a dynamic equation to determine number of filaments at the rear of the object 2) a force balance equation as shown in figure 3-1 and 3) constitutive relations to describe the force and dissociation rate.

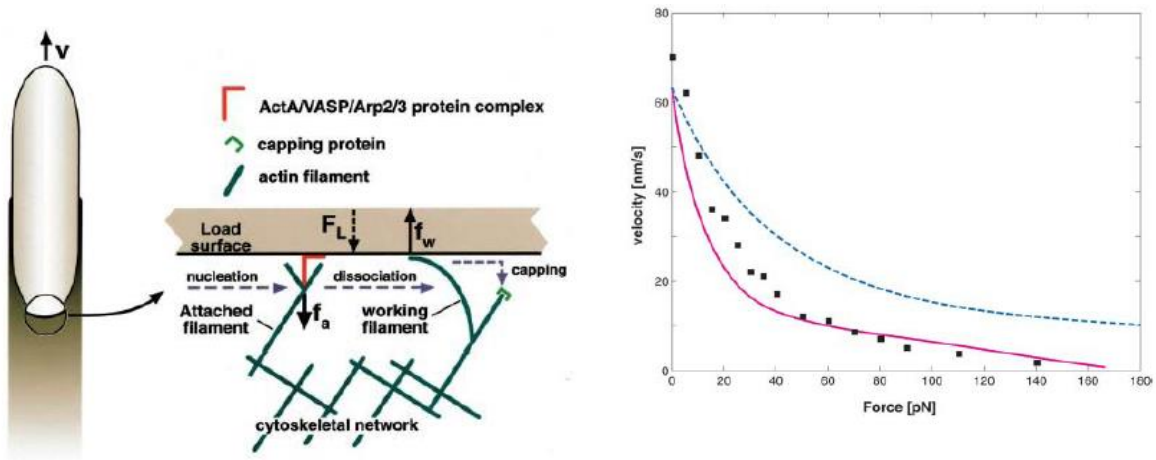


Figure 3-1 Schematic of the TBR model proposed by Mogilner and Oster (2002) and the predicted force-velocity profile [23] © 2003 by the Biophysical Society.

1. In order to study actin dynamics for the whole process, several parameters and variable are defined:

The number of the filaments attached to the surface via the surface protein (ActA/WASP), a , which depends on the nucleation rate of actin monomers and dissociation rate of the attached filaments: $\frac{da}{dt} = n - \delta a$, where n is the nucleation rate of

the attached filaments with the assumption that new filaments are nucleated and branched

out from the tip and/or sides of the existing filaments; and δ is filament dissociation rate and depends on the object movement velocity.

The number of dissociated or ‘working’ filaments (which are polymerizing and generating the propulsive force, w), depends on the dissociation rate and the capping rate:

$$\frac{dw}{dt} = \delta a - \kappa w, \text{ where } \kappa \text{ is the capping rate of the growing filaments.}$$

Another assumption is that the number of nucleation sites on the surface is constant (e.g. the surface area of the object is limited and a fixed number of filaments can tether to it) and therefore the nucleation rate is not changing. Since the molecular details of the actin dynamics are not clearly understood, the formulated model is kept simple.

2. A simple force balance between the forward pushing force generated by working filaments and the tensile force of the attached filaments along with other forces that might resist the movement of the object will result in: $F_L + f_a a = f_w w$ where F_L is the total dissipative and conservative load force including the viscous drag force on the cell as well as any external force, while f_a and f_w are the force of attached and working filaments respectively. Another assumption here is to assume that the comet tail will be firmly cross-linked to the cytoskeleton of the cell therefore any force other than the elastic recoil of the tail near the surface of object, will not enter the force balance equation.
3. Since the force of attached and working filaments as well as the dissociation rate are functions of the moving velocity, a force-velocity relationship is defined to evaluate the dependency of the propulsive force to the propulsion velocity. Previously, it had been shown that object velocity depends on the polymerization and depolymerization velocities through the following equation:

$$V = V_{\max} \exp\left[\frac{-f_w l}{k_B T}\right] - V_{\text{dep}}, \text{ where } V_{\max} \text{ and } V_{\text{dep}} \text{ are the free polymerization velocity and}$$

the depolymerization velocity, respectively. l is the growth of filament upon one monomer addition and is equal to the half size of an actin monomer and $k_B T$ is thermal energy (~ 4.1 pN.nm). Here, the EBR model assumes that the depolymerization rate is not affected by the moving velocity, but the polymerization rate will decrease exponentially with the force. Another assumption is that the elastic recoil of the meshwork does not introduce major effects on the force velocity relationship of a single filament, therefore the same equation can be used for estimation of the growth rate of the actin network.

In steady state propulsion, the number of working and attached filaments can be determined by the following equations: $a(v) = n / \delta$ and $w(v) = n / \kappa$. The number of attached and working filaments at each time is a function of the velocity of the object. However, the total number of filaments at the rear of the object is only a function of the number of available nucleation sites on the surface and is constant. With these equations, it is clear that the ratio of the working and attached filaments is not a function of the nucleation rate which as discussed in the next section will help us to estimate some of the parameters in the model.

The dissociation rate of the filaments is also affected by the load force and the velocity of the object. With no force applied, dissociation will be spontaneous with the free dissociation rate δ_0 . However, upon application of a constant force, the dissociation rate will change as an exponential function of the applied force: $\delta = \delta_0 \exp(f / f_b)$ where f is the applied force and f_b is the effective strength of the attachment bond. The applied force to the attachment bond can be expressed as a force applied to a series of springs (representing flexible filaments) which is a function of the object's moving velocity.

We introduce a dimensionless velocity $v \equiv V/V_0$, with $V_0 = f_b \delta_0 / k$ and k being the spring coefficient of the transducer springs representing the actin filaments. The velocity dependency of the parameters can be defined as:

$$\delta(v) = \delta_0 / \omega(v) \quad \text{Eq 3-1}$$

$$f_a(v) = f_b \cdot \omega(v) \cdot v \quad \text{Eq 3-2}$$

where $\omega(v) = \int_0^\infty dx \cdot x \cdot \exp[vx + \frac{1 - \exp(vx)}{v}]$ with asymptotic behavior of $\omega(v) \approx 1$ for $v \ll 1$ and $\omega(v) \approx \ln(v) / v$ for $v \gg 1$. In the case when the movement is very slow, the dissociation rate is almost equal to the free dissociation rate and the force due to attached filaments is proportional to the propulsion rate. On the other hand, with a very fast moving object, the effective dissociation rate increases with the velocity in a sub-linear way and therefore the detachment force decreases slowly.

Substituting all the equations given above into the velocity equation, we can estimate the rate of propulsion and study the driven force-velocity relationship:

$$V = V_{\max} \exp[-l(f_a(a/w) + (F_L/w)) / k_B T] - V_{dep} \quad \text{Eq 3-3.a}$$

or

$$V = V_{\max} \exp[-l(f_b v \omega^2(v)(\kappa / \delta_0) + (F_L \kappa / n)) / k_B T] - V_{dep} \quad \text{Eq 3-3.b}$$

or in dimensionless form: $v = \varepsilon_2 \exp[-\varepsilon_1 v \omega^2(v) - \varepsilon_4] - \varepsilon_3$ where $\varepsilon_1 = (f_b l / k_B T)(\kappa / \delta_0)$, $\varepsilon_2 = (V_{\max} / V_0)$, $\varepsilon_3 = (V_{dep} / V_0)$ and $\varepsilon_4 = (F_L l / k_B T)(\kappa / n)$ represents work done by each of the working filaments to break attachment, the free polymerization velocity, the free

depolymerization velocity and the work done by the external force on each working filaments; respectively.

3.2 Model parameters

The value of the key dimensional parameters of the model e.g. monomer size, thermal energy and the strength of the attachment bond can be extracted from literature. These parameters only depend on the actin monomer features so the values from [23] can be implemented in our model. ($l=2.2$ nm, $k_B T \sim 4.1$ pN.nm and $f_b=10$ pN). The other parameters are unknown and in this section we will estimate those values to the best of our knowledge comparing them with experimental observations.

1. V_{max} is the free polymerization rate and depends only on the concentration of the G-actin monomers available for polymerization. According to Pollard et al. [10], this concentration depends on the type of the cell but mostly <100 μ M. Therefore the value of ~ 500 nm/s suggested by [23] can also be used in the baculovirus case.
2. k is the transducer spring coefficient of the weakest spring. It can be ~ 0.1 pN/nm for a 200-nm long bending filament, or it can also be in the order of 10 pN/nm for the longitudinally stretched filaments, according to Mogilner and Oster. (Values are comparable with those suggested by [26], $k_C=0.17$ pN/nm and $k_T=60$ PN/nm). Mogilner and Oster had suggested taking an intermediate value (e.g. 1pN/nm [23]) for this spring constant which is in the order of characteristic elastic constant of the protein spring suggested by [61]. Since this spring constant depends on the filament features, the same value is applicable in baculovirus case.
3. V_{dep} is the actin depolymerization velocity which only depends on the rate of the monomer disassembly, but Mogilner and Oster suggested different values. In [23] the

depolymerization velocity depends on the monomer length and the rate of monomer disassembly and is ~ 2.2 nm/s. On the other hand in [31] the depolymerization speed is 388 nm with an aging rate parameter of 555/s (both of which are obtained using fitting parameter) This translates to a depolymerization rate of ~ 0.7 nm/s for the case of the baculovirus. Since the latter case is obtained by fitting parameters, for *Listeria* for our model we will use the value extracted from literature and reported by Mogilner.

4. n is the nucleation rate which depends on the number of nucleation sites on the motile surface. Given the smaller dimensions of baculovirus compared to *Listeria*, one may expect a proportionally smaller n . For *Listeria* the total number of filaments near the surface of the object is tens to hundreds and therefore taking the lower limit of number of filaments for baculovirus with smaller size, the estimated value of nucleation rate will be $n=10/s$, which matches the value of 9.4/s suggested by parameter fitting in Mueller *et al.* study [31].
5. In order to estimate capping rate and free dissociation rate the following arguments were considered and both parameters are estimated simultaneously to match the observed velocity of baculovirus inside the host cell:

κ is the capping rate and can be estimated based on the observed filament length and moving velocity of the object. Suggesting a filament length of tens to hundreds nm and reporting an object velocity of the same order of magnitude (i.e. tens to hundreds nm/s), Mogilner and Oster ended up using κ in the order of 1/s. However, Mueller et al. had suggested a capping rate of 6.4/s obtained by parameter fitting for the case of baculovirus propulsion. Note that this value is obtained based on the observed (maximum) moving velocity of ~ 50 $\mu\text{m}/\text{min}$ and average filament length of $\sim 120\text{nm}$ [31]. However this

velocity is much higher than those observed for baculoviruses experiments: (7-22 $\mu\text{m}/\text{min}$ or average of $\sim 14\mu\text{m}/\text{min}=233\text{ nm/s}$ [1, 62]). Using the value reported by Mueller et al. the velocity predicted by the model is not within a reasonable range of experimental values. The value of capping rate can be estimated using the fact that $\kappa = vL$ and v is also given by the model as $v = \varepsilon_2 \exp(-\varepsilon_1 v \omega^2(v) - \varepsilon_4) - \varepsilon_3$. Therefore, we need to find the κ value for which the following is satisfied:

$$v = \frac{\kappa}{L} = \varepsilon_2 \exp(-\varepsilon_1 v \omega^2(v) - \varepsilon_4) - \varepsilon_3 \quad \text{Eq 3-4}$$

where L is the length of the comet tail observed for the virus and is $\sim 120\text{ nm}$ [31]. Solving this equation yields $\kappa=2/\text{s}$, which predicts a steady state velocity of $\sim 230\text{nm/s}$. Note that this estimated value also varied with the choice of free dissociation rate as discussed below

δ_0 or the free dissociation rate has been considered in the order of $1/\text{s}$ by Mogilner and Oster to ensure stable and fast locomotion of the object by actin propulsion. This value gives $\kappa=0.8/\text{s}$ and $V_{\text{predicted}} = 77.4\text{ nm/s}$ (much less than the expected velocity for the virus). δ_0 was assumed to be $\sim 2.7/\text{s}$ by [32]. This value gives $\kappa=1.3/\text{s}$ and $V_{\text{predicted}} \sim 155\text{ nm/s}$. Since there is no actual measurement of this parameter in literature, it can be chosen so as to give the best match between the predicted values from model and observed values in the experiments. For the value of $\delta_0 = 6.3/\text{s}$ all the above mentioned criteria is satisfied and the model will predict the moving velocity within acceptable range.

The parameter values discussed above are summarized in the table 3-1.

Table 3-1 Summary of the parameters of actin propulsion model

parameter	definition	value	justification
V_{max}	free polymerization rate	500 nm/s	[23]
V_{dep}	actin depolymerization velocity	2.2 nm/s	[23]
k	transducer spring coefficient	1 pN/nm	[23]
n	nucleation rate	10 /s	[23, 31]
$\delta\theta$	free dissociation rate	6.3 /s	calculated based on a , w and κ
κ	capping rate	2 /s	calculated based on filament length and observed velocity of the object [31]
l	monomer length	2.2 nm	[23]
x_b	effective length of attachment bond	0.4 nm	[23]
f_b	effective strength of attachment bond	10 pN	[23]

3.3 Model predictions

The model predicts the movement of the virus as result of actin comet tail formation and growth at the back of it. Solving equation 2-4 with the parameter values discussed above, the steady state velocity of the virus can be determined in the case of no external force applied. For the given parameters, the value of dimensionless model parameters, V_0 , and ϵ_1 - ϵ_4 are 63 nm/s, 1.7, 7.93, 0.03 and 5.47; respectively. The numerical solution of Eq. 3-4 gives a steady state

velocity of ~230 nm/s which matches very well the expected moving velocity of the baculovirus observed in the experimental studies [1, 62].

The right hand side of Eq. 3-4 has two different behaviors in the fast and slow ranges for velocity. For the slower velocities, the dissociation rate is constant and force of attachment is proportional to the velocity; whereas for the faster velocities the attachment force resisting the working filaments increases slowly with the velocity and the change in the dissociation rate is dominant. The unique solution for steady state with no external force happens at $v=3.66$, which translates to a propulsion velocity of 230 nm/s. Using equations 3-1 and 3-2 for the steady state velocity we have the effective dissociation rate of 6.3 /s and attachment force of 36.6 pN. This implies the molecular link between attached filaments and the motile surface breaks 6 times faster when the object is moving fast under steady state conditions. This also implies that at any given point during polymerization the ratio of the working to attached filaments is 6 and the average force of the working filaments will be ~6 pN.

For the next step, we compute the force-velocity profile for the baculovirus riding on the actin comet tail by solving equation 2-4 with the same parameter values while varying external load force to see when the virus's movement stall. In this case, upon application of the external load force, the number of attached filaments increases and the movement stalls at the force value of ~50 pN. The predicted force-velocity profile has 2 distinct zones (figure 3-2): at small loads, the velocity drops down very quickly because of the rapid breaking of the attachments and the tensile force from the attached filaments is very small. In this case a positive feedback system reduces the velocity very quickly due to the longer attachment of the filaments to the motile surface in slow regime. The longer filaments stay attached to the motile surface, the higher the effective drag would be which further reduces the speed of the object. However, in case of very

large values of force, the filament attachment will break with a rate equal to the free dissociation rate and there will be less force per attachment in lower velocity. Unlike the case of the fast movement where most of the resistance was from the attached filaments, in this zone, the resistance of the external force is dominant and therefore the velocity drops at slower rate compared to the first zone.

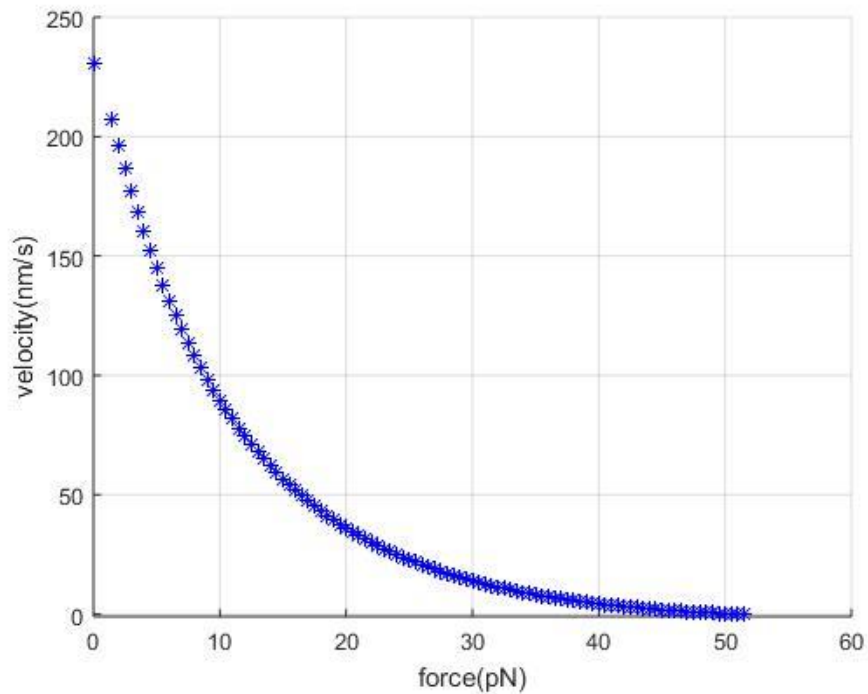


Figure 3-2. The predicted force- velocity profile of the baculovirus riding on the actin comet tail.

The model predicts a stalling force of 50 pN for the baculovirus nucleocapsid. This value remains to be checked against experimental measurements, which do not exist at present. Experimental observations of the baculovirus entering the cell nucleus shows that the actin polymerization force is large enough that can actually bend the nuclear envelope of the cell and pushes the virus through [1, Video 7]. Conceivably an estimation of the force can be obtained

from the bending modulus of the nuclear envelope. Another recent study on actin-based propulsion shows a very distinct role of actin polymerization force not only in cytoplasmic migration of the baculovirus nucleocapsid, but also in the NPC entry of it [63]. The generated force to a great extent depends on the model parameters and the selection of the parameters in our model might be the reason for the lower level of the predicted force.

Chapter 4: Nucleus entry of the baculovirus

As reviewed in chapter 2, several different modeling approaches were developed to describe the selective permeability function of the NPC central channel. In this thesis, the baculovirus entry to the NPC central channel is modeled using a continuum model. As mentioned in chapter 2, the NPC channel can be modeled as a saturated hydrogel made of FG-regions of the nups [54]. In this model, in order for the baculovirus to enter the nucleus, it needs to break through the gel structure. This phenomenon has been studied widely in the context of solid mechanics of a sharp or blunt needle punching into a soft solid. To understand the nature of soft solid penetrations and the underlying mechanism of mechanical puncture, several different models have been developed. Here, we apply one of these mechanical penetration models to the case of NPC gel being punched into by a baculovirus.

Evidences suggest that the penetration of a needle-like object into the soft solid involves cracking followed by reversible deformation of the gel [64]. A number of experimental studies have examined the correlation between the crack size and shape and the punch tip geometry and material properties of the gel [65, 66]. Some other studies focused on measuring the force required for the deep penetration and its dependency of the sharpness of the punch as well as the speed of penetration [67, 68]. In their micromechanical models of soft solid penetration, Shergold & Fleck in 2004 [64], developed a constitutive description for the stress-strain responses of a different soft materials punched with sharp- and flat-ended punches. They defined the crack geometry in such a way as to minimize the load for the steady state penetration and calculated the required force as a function of material properties and punch diameter [64].

4.1 Deep penetration of a punch into a soft solid

4.1.1 Penetration of flat-ended punch

Penetration of a soft hyperelastic solid by a flat-bottomed cylindrical punch can be studied using the Ogden formulation of strain energy density

$$\phi = \frac{2\mu}{\alpha^2}(\lambda_1^\alpha + \lambda_2^\alpha + \lambda_3^\alpha - 3) \quad \text{Eq 4-1}$$

where ϕ is the strain energy density per undeformed unit of volume, α is the strain hardening exponent of the solid, μ is shear modulus under infinitesimal straining and λ_i are the principal stretch ratios). Assuming the flat-ended punch being frictionless and rigid, we consider a ring crack propagating ahead of the punch tip as in Shergold and Fleck [64]. The model assumes a crack of radius b and length l enclosing in the undeformed state of the material, which is then compressed to the length $l-h$ (after punch advancing h units) and radially expanded from b to R to accommodate the punch. Therefore, the total work required for advancing the punch into the solid is the sum of the work required for making a crack of width b , the work required for compressing the crack underneath the punch tip, and the work required for radial expansion of the column (Figure 4-1).

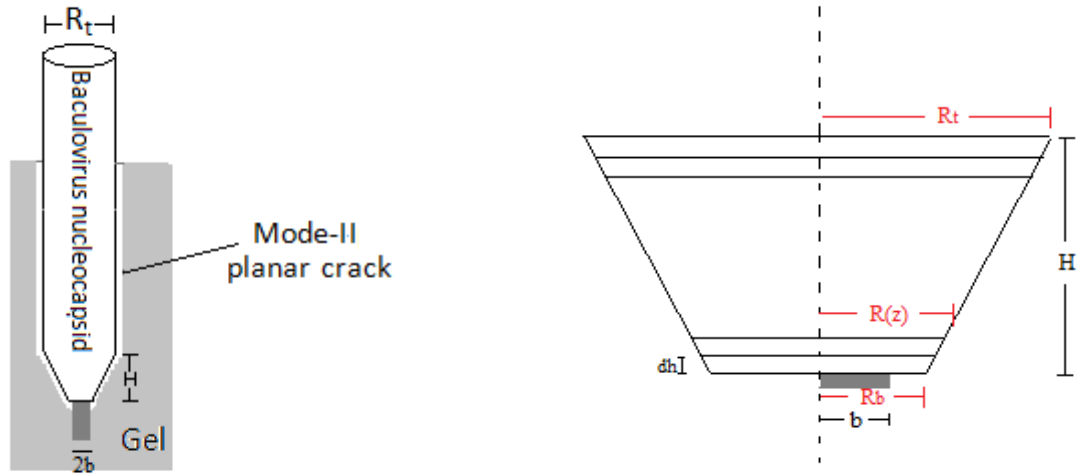


Figure 4-1 Left) Schematic of the flat-ended punch penetrating into the soft solid. Compressed column of radius $b < R_b$ is shown in darker grey color. Right) Schematic of the infinitesimal layers of increasing radius in the tip of the Baculovirus.

1. Crack formation energy:

$F_{crack} = 2\pi b J_{IIC}$ where J_{IIC} is the toughness of the material to the mode II crack propagation.

2. Column compression energy:

For an incompressible material, the principal stretch ratios can be defined for any given undeformed state changing to the deformed compressed state:

$$\frac{\partial S_C}{\partial l} = \frac{2\mu\pi}{\alpha^2} R_b^2 \left[2\left(\frac{b}{R}\right)^{2-\alpha} + \left(\frac{b}{R}\right)^{2\alpha+2} - 3\left(\frac{b}{R}\right)^2 \right] \quad \text{Eq 4-2}$$

3. Hole expansion energy:

When the stress-strain response of a material is given by the strain energy function, a simple method to calculate this energy can be implemented.

$$\frac{\partial S_H}{\partial l} = \frac{2\mu\pi}{\alpha^2} R_b^2 \int_1^\infty \left(\left(1 - \frac{(\frac{b}{R_b})^2}{\eta}\right)^{\alpha/2} + \left(1 - \frac{(\frac{b}{R_b})^2}{\eta}\right)^{-\alpha/2} - 2 \right) d\eta \quad \text{Eq 4-3}$$

Therefore the magnitude of the total force required for advancing the flat punch by δl increment is given by:

$$P_F = \left[F_{crack} + \frac{\partial S_C}{\partial l} + \frac{\partial S_H}{\partial l} \right] \left(\frac{\partial l}{\partial h} \right) \quad \text{Eq 4-4}$$

For details on how each of these energies is defined, refer to Shergold and Fleck [64]. So the three terms contribute to the total force. Investigating the contribution of each term, Shergold and Fleck defined an optimized b/R ratio which minimizes the required punching load. This will obviously be a function of material properties and the diameter of the punch. The higher the toughness is the smaller the crack can be formed in it. On the other hand, the smaller the punch size the bigger the needed crack. Evaluating a wide range of toughness and strain hardening values along with different punch sizes, Shergold and Fleck predicted an increasing force with increase the material toughness and decreasing the punch diameter (Figure 4-2).

REMOVED BECAUSE THE PERMISSION FROM COPYRIGHT OWNERS IS NOT RECEIVED. **REMOVED BECAUSE THE PERMISSION FROM COPYRIGHT OWNERS IS NOT RECEIVED.**

Figure 4-2 Right) The punching pressure profile versus non-dimensionalized $J_{IC}/\mu R$ parameter; Left) The minimum crack opening versus non-dimensionalized $J_{IC}/\mu R$ parameter, for the flat-ended punch [64].

4.1.2 Penetration of sharp-ended punch

The other case studied by Shergold and Fleck is the deep penetration of a sharp-ended punch where they considered a frictionless rigid sharp punch with a conical tip advancing into a semi-infinite block of elastic material. For this case, they assume there exists a crack of width $2a$ on the surface of the material which will tear and open at the tip of the punch. Assuming a plane-strain crack in a slice of length δl , the steady state advance of the punch will require energy to form the crack and the energy to open the crack and accommodate the cylinder (Figure 4-3).

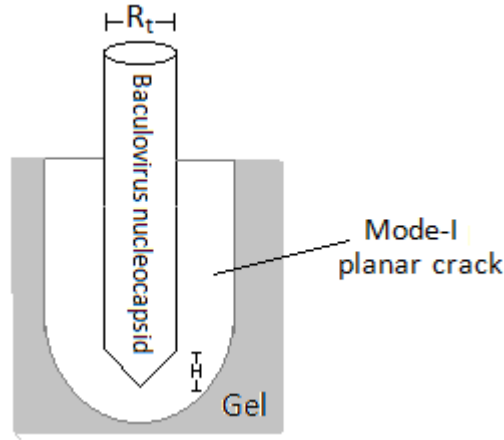


Figure 4-3 Schematic of the flat-ended punch penetration into the soft solid.

1. Crack formation energy:

$$\delta W_c = 2J_{IC} a \delta l, \text{ where } J_{IC} \text{ is the mode I toughness of the material.}$$

2. Stored strain energy:

The work required to open the crack and expand the pre-existing crack from 0 width to the radius of the punch is given by:

$$\delta S_E = \mu R_b^2 h \left(\frac{a}{R} \right) \delta l, \text{ where } h \left(\frac{a}{R} \right) \text{ is a dimensionless function evaluated explicitly by}$$

finite-element procedure and only depend on the strain-hardening exponent (α) of the gel.

Reading the data from the p_s/μ curve of Shargold and Fleck [64] and using a curve-fitting tool, the universal function of h is given by:

$$\frac{p_s}{\mu} = \frac{P_s}{\mu\pi R^2} = \frac{2}{\pi} \frac{J_{IC}}{\mu R} \frac{a}{R} + \frac{1}{\pi} h\left(\frac{a}{R}\right) \quad \text{Eq 4-5}$$

with

$$h\left(\frac{a}{R}\right) = \pi(0.6\left(\frac{a}{R}\right)^{-1.22} + 0.4) = 1.9\left(\frac{a}{R}\right)^{-1.22} + 1.3 \quad \text{Eq 4-6}$$

The total force required for this penetration will be given by:

$$P_s = 2J_{IC}a + \mu R^2 h\left(\frac{a}{R}\right) \quad \text{Eq 4-7}$$

Similar to the flat-ended punch model, this total force can be minimized by an optimized value of crack width (a). a is smaller for tougher materials and/or smaller punch sizes. Evaluating several cases Shergold and Fleck [64] predicted minimum punching force increases with an increase to the toughness of material and decrease in punch size (Figure 4-4).

REMOVED BECAUSE THE PERMISSION FROM [REDACTED] COPYRIGHT OWNERS IS NOT RECEIVED. [REDACTED] COPYRIGHT OWNERS IS NOT RECEIVED.

Figure 4-4 Right) The punching pressure profile versus non-dimensionalized $J_{IC}/\mu R$ parameter; Left) The minimum crack opening versus non-dimensionalized $J_{IC}/\mu R$ parameter, for the sharp-ended punch [64].

Here, considering the NPC gel as an incompressible [69], hyperelastic [70] and isotropic [47] material, we can easily apply the assumptions of Shergold & Fleck's model to the case of baculovirus penetration. Two different scenarios are investigated and the punching load is calculated for each of them: 1. A blunt conical tip punch 2. A sharp tip punch. Since both models in their original form of [64] dealt only with the steady-state penetration, we will need to generalize them to account for the geometry of the conical tip of the virus.

4.2 Baculovirus penetration into the soft gel on NPC central channel

4.2.1 Blunt conical tip baculovirus

Baculovirus is a rod like structure with an apical cap end with a small protuberance and a blunt end. Its nucleocapsid ranges from 250-300 nm in length and 30-60 nm in diameter [5]. The tip of the nucleocapsid has an opening angle of 75° and its diameter at the tip as measured by image analysis is 7-10 nm (average of 6 measurements on the same image) (figure 4-5). Therefore we may take $R_b = 3.5$ nm to be the radius of the blunt tip. The diameter of the baculovirus nucleocapsid is reported to be 30-60 nm [5], so $R_t = 15$ nm. At present, we have used the lower limit of the size reported for baculovirus. Later we will update the model with the larger sizes as well. The sloped conical surface can be modeled as a series of infinitesimal layers with increasing radius. So in the modified version of the flat end model, there will be a fourth term added to the force contributions to account for the tip.

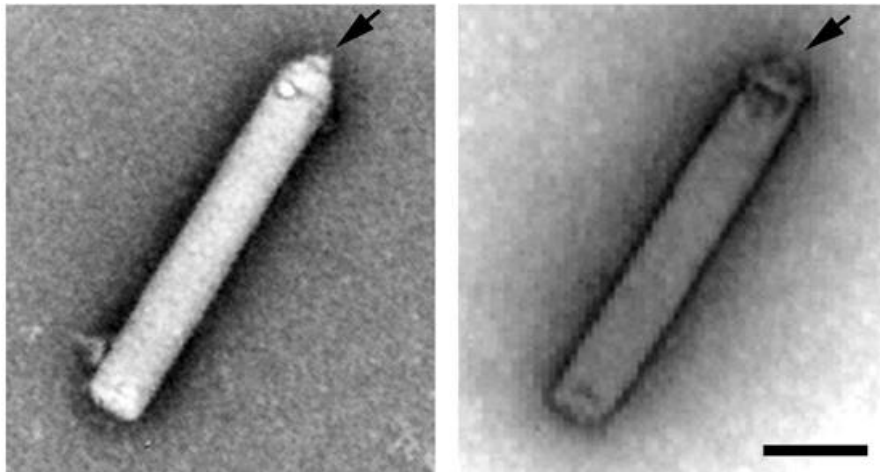


Figure 4-5 Electron micrographs of the baculovirus nucleocapsid, showing the morphology of the nucleocapsid with its two distinct ends; a blunt end and a conical end with a small protuberance. Scale bar is 50 nm (Printed from [3] © 2011 Elsevier Inc.).

For this, infinite layers of the punch with different radii have been evaluated. These layers create a radial expansion of the hole generated by the very bottom layer (with smallest radius) to the very top layer (with maximum radius).. Considering one such infinitesimal layer of the punch advancing by dh step increments, the radius of the punch will increase from $R(z)$ to $R(z)+dhtan(\theta)$ where $R(z)$ is the radius of the previous layer and $\theta=75^\circ$ is the half opening angle of the tip (Figure 4-1).

For each layer the additional energy required to accommodate the next wider layer is given by:

$$\frac{dS}{dh} = \int_b^\infty 2\pi r dr [\phi(r, R(z) + dhtan(\theta)) - \phi(r, R(z))] \quad \text{Eq 4-8}$$

Where ϕ is the one-term Ogden strain energy density function for the hyperelastic material introduced earlier.

Adding the integral for all the layers in the tip, the following will be obtained which can be evaluated numerically to find the force required for this expansion.

$$\frac{dS}{dh} = \int_{R(\text{bottom})}^\infty 2\pi r dr [\phi(r, R(\text{top})) - \phi(r, R(\text{bottom}))] \quad \text{Eq 4-9}$$

Plugging in the strain energy equation into the integral: ($R(\text{top})= R_t$ and $R(\text{bottom})= R_b$)

$$\frac{dS}{dh} = \frac{2\mu}{\alpha^2} \left(\int_{R_t}^\infty 2\pi r dr \left(\left(\frac{r(\text{top})}{s} \right)^\alpha + \left(\frac{r(\text{top})}{s} \right)^{-\alpha} - 2 \right) - \int_{R_b}^\infty 2\pi r dr \left(\left(\frac{r(\text{bottom})}{s} \right)^\alpha + \left(\frac{r(\text{bottom})}{s} \right)^{-\alpha} - 2 \right) \right)$$

Eq 4-10

Using volume conservation for incompressible gel s can be rewritten in terms of r and $R(z)$ as $s^2 = r^2 - R^2 + b^2$. Substituting this in, the integral will be:

$$\frac{dS}{dh} = \frac{2\mu}{\alpha^2} \left[\int_{R_t}^{\infty} 2\pi r dr \left(\left(\frac{r^2 - R_t^2 + b^2}{r^2} \right)^{\frac{\alpha}{2}} + \left(\frac{r^2 - R_t^2 + b^2}{r^2} \right)^{\frac{-\alpha}{2}} - 2 \right) - \int_{R_b}^{\infty} 2\pi r dr \left(\left(\frac{r^2 - R_b^2 + b^2}{r^2} \right)^{\frac{\alpha}{2}} + \left(\frac{r^2 - R_b^2 + b^2}{r^2} \right)^{\frac{-\alpha}{2}} - 2 \right) \right] \quad \text{Eq 4-11}$$

Evaluating this integral numerically along with the other three terms results in the following force values depending on choice of parameters in the other 3 terms. Therefore, the mechanical properties (e.g. toughness, shear modulus and strain hardening coefficient) of the NPC gel needs to be evaluated.

$$P_F = \left(1 - \left(\frac{b}{R}\right)^2\right)^{-1} \left[2\pi b J_{IC} + \frac{2\mu\pi}{\alpha^2} R_b^2 \left[2\left(\frac{b}{R_b}\right)^{2-\alpha} + \left(\frac{b}{R_b}\right)^{2\alpha+2} - 3\left(\frac{b}{R_b}\right)^2 \right] + \frac{2\mu\pi}{\alpha^2} R_b^2 \int_1^{\infty} \left(\left(1 - \frac{\left(\frac{b}{R_b}\right)^2}{\eta}\right)^{\alpha/2} + \left(1 - \frac{\left(\frac{b}{R_b}\right)^2}{\eta}\right)^{-\alpha/2} - 2 \right) d\eta + \frac{2\mu}{\alpha^2} \int_{R_t}^{\infty} 2\pi r dr \left(\left(\frac{r^2 - R_t^2 + b^2}{r^2} \right)^{\frac{\alpha}{2}} + \left(\frac{r^2 - R_t^2 + b^2}{r^2} \right)^{\frac{-\alpha}{2}} - 2 \right) - \frac{2\mu}{\alpha^2} \int_{R_b}^{\infty} 2\pi r dr \left(\left(\frac{r^2 - R_b^2 + b^2}{r^2} \right)^{\frac{\alpha}{2}} + \left(\frac{r^2 - R_b^2 + b^2}{r^2} \right)^{\frac{-\alpha}{2}} - 2 \right) \right] \quad \text{Eq 4-12}$$

4.2.2 Blunt conical tip baculovirus – modified model

Applying the above model to the case of baculovirus (i.e. very thin punch) shows a great contribution from the tip term, implying very small values of b to minimize the punching force. This is because the fracture toughness J of the NPC hydrogel combined with the small diameter

of the virus yields a very small b_{\min} , below 0.01 nm. There is no physical meaning in having a crack size smaller than an atom. This implies Shergold and Fleck's continuum flat-ended model does not apply for our situation, which has such a thin "needle". An alternative to this model would be omitting the details of how a small crack of size b is created, and how it is compressed vertically and expanded radially. Instead, we imagine a circular crack of radius R_b and depth (δh) being created, and then expanded along the conical surface to R_t . In this picture, the total energy required for puncturing the gel has only two energy terms: the fracturing energy, and the expansion energy from R_b to R_t . This modified model will result in:

$$\frac{dS}{dh} = \frac{2\mu}{\alpha^2} \int_{R_t}^{\infty} 2\pi r dr \left(\left(\frac{r^2 - R_t^2 + R_b^2}{r^2} \right)^{\frac{\alpha}{2}} + \left(\frac{r^2 - R_t^2 + R_b^2}{r^2} \right)^{\frac{-\alpha}{2}} - 2 \right) \quad \text{Eq 4-13}$$

$$P_F = \left[2\pi b J_{IC} + \frac{2\mu}{\alpha^2} \int_{R_t}^{\infty} 2\pi r dr \left(\left(\frac{r^2 - R_t^2 + R_b^2}{r^2} \right)^{\frac{\alpha}{2}} + \left(\frac{r^2 - R_t^2 + R_b^2}{r^2} \right)^{\frac{-\alpha}{2}} - 2 \right) \right] \quad \text{Eq 4-14}$$

So evaluating the contribution of these two terms will give us a rough estimate for the required force for punching the NPC gel with the thin baculovirus.

4.2.3 Sharp conical tip baculovirus

The sharp model of Shergold and Fleck also considers the steady state penetration of the punch into the solid and does not account for the penetration of the conical tip part. In other words, they assume the conical tip has already penetrated completely, and there is no longer a change in radius as the punch penetrates further. Therefore, in order to account the force required for advancing the tip of increasing radius into the gel, we suggest a modified version of the model evaluating the two term of the force using integration method.

The equation for strain energy $\delta S_E = \mu R_b^2 h(\frac{a}{R}) \delta l$ implies:

$$S_E = \int_0^H \mu R(z)^2 h(\frac{a}{R}) dz \quad \text{Eq 4-15}$$

Where H is the length of the tip of the virus: $H = \frac{R}{\tan(\theta)} = \frac{15}{\tan(75)} = 4(nm)$.

As mentioned earlier, a is optimized to give the minimum punching force, therefore in the above integral form, the ratio $\frac{a}{R}$ remains the same at different z locations. $R(z)$ can be expressed in terms of the depth of the conical tip inside the gel and θ (the half angle of the opening of the conical tip, which is 75° for baculovirus).

$$S_E = \int_0^H \mu R(z)^2 h(\frac{a}{R}) dz = h(\gamma) \mu \int_0^H (z \tan(\theta))^2 dz = h(\gamma) \mu \tan^2(\theta) \frac{H^3}{3} \quad \text{Eq 4-16}$$

On the other hand the crack formation energy for the conical tip can be calculated as:

$$W_c = 2J_{IC} \gamma H \tan(\theta) \quad \text{Eq 4-17}$$

Therefore the punching force required for the tip is as below:

$$F_{s_tip} = h(\gamma) \mu \tan^2(\theta) H^2 + 2J_{IC} \gamma \tan(\theta) \quad \text{Eq 4-18}$$

This force value will depend on the depth of the penetration of the tip. Using the mechanical properties (e.g. toughness, shear modulus and strain hardening coefficient) obtained in the next sections, we can evaluate the total load required.

4.3 Mechanical properties of the NPC gel

For all of the models presented above, we need to know toughness, shear modulus and strain hardening properties of the NPC gel. This section will focus on the mechanical properties of the NPC gel as extracted or inferred from the literature.

4.3.1 Shear modulus of the NPC gel

Different studies have measured the mechanical properties and Young's modulus of the NPC. In an attempt to measure the elasticity of in-vitro FG hydrogel, Frey et al, [54] synthesized a gel of 26 mg of FG repeats into 1 ml of homogeneous aqueous solution which showed an elasticity of 1-2 kPa [54]. However this in-vitro gel is not saturated with FG repeats and does not show the selective permeability of the NPC hydrogel. In later investigations, Frey et al [55] showed that in order for the gel to show the selectivity for NTR cargos and other larger molecules, the gel need to be saturated with concentrations of FG domain almost 10 times higher (~200 mg/ml) [55]. However, in this later study, they did not investigate the mechanical properties and elasticity of the gel.

Recently Bestembayeva et al [69] used a sharp-tip AFM cantilever to study the force-indentation profile of NPC central channel and reported an elasticity value of 1-2 MPa (depending on the geometry of the sharp tip e.g. conical vs. spherical) for it. These measurements are good representatives of NPC mechanical properties, since they extracted nuclear envelopes from *X. laevis* oocytes and carried out the AFM indentation tests without any fixation [69]. In another study, the Young's modulus of *in-vitro* films made of FG repeat domains of the yeast nucleoporin Nsp1 was measured by AFM and reported to have a value of 0.15 MPa [70]. Shear modulus (μ) of any homogeneous isotropic material can be calculated from

its Young's modulus using $\mu = \frac{E}{2(1+\nu)}$. Since the NPC gel is considered to be incompressible,

Poisson's ratio $\nu=0.5$ and therefore the shear modulus is $\mu=0.05$ MPa.

4.3.2 Toughness of the NPC gel

Since the NPC channel is an intracellular organelle and hard to access, there are not many studies focusing on direct measurements of the mechanical behavior and in particular toughness of the gel. Reviewing several different hydrogel materials in the literature, we decided to approximate the desired properties of the NPC gel with the most similar synthetic gel in terms of the molecular weight and stiffness. As listed in table 4-1 the toughness values for different gel materials range from 1 J/m³ to 5500 kJ/m³ and among all these materials, agarose has the molecular weight and Young's modulus in the range of those for the NPC gel. Note that this matching also depends on the polymer concentration of agarose. Therefore, agarose is chosen to represent the NPC gel.

Table 4-1 Summary of the gel toughness and other properties of the *in vitro* hydrogels

Gel	Solid content	E	Crosslink density	M _w	M _c (b/t crosslinks) g/mol	Toughness
FG-nups	26 mg/ml equivalent to .4% agarose	1-2 kPa [54]	-	65 kDa [70] 65000 g/mol	-	To be approximated
	Real NPC, sharp-tip AFM measurement	1-2 Mpa [69]				
	FGRD film, AFM micorindentation	0.15Mp a [70]				

Gel	Solid content	E	Crosslink density	M _w	M _c (b/t crosslinks) g/mol	Toughness
Agarose	2.25% [71]	28 kPa [71]	0.32 M [71]	120000	3700 [71]	0.2 kJ/m ³ [71]
PEG	7.34% [71]	36 kPa [71]	0.069 M [71]		10900 [71]	37 kJ/m ³ [71]
PEGDA (diacrylate) [72]	10%	24.4 kPa	9.82 mol/m ³	-	1020	21.6 kJ/m ³
	10% +2.5%	28 kPa	11.3 mol/m ³		1790	46.3 kJ/m ³
	10% + 5%	27.5 kPa	12 mol/m ³		675	93.4 kJ/m ³
	10% +10 %	37.9 kPa	15.3 mol/m ³		179	254.21 kJ/m ³
Polyacrylamide (PAM)	40% [73]	-	-	Acryl: 71.08 Bas: 154.1 7	-	66.9 kJ/m ³ [74]
	5/0.025 [75]	4.3 kPa				
	22% [76]	0.05 kPa				
poly(2-acrylamide-2-methylpropane sulfonic acid) PAMPS/PAM* [77]	13 %	0.158 MPa	0.8 M*	71.08 Acr 207.2 4 amps	-	1250 J/m ³

Gel	Solid content	E	Crosslink density	M _w	M _c (b/t crosslinks) g/mol	Toughness
PAMPS/PAM_PEG [77]	w 0.4% PEG w 0.8% PEG	0.124 0.133	0.9 M*	20000 PEG 71.08 Acr 207.2 4 amps	-	1220 1216
alginate-polyacrylamide hydrogels [78]	14% solid 80 % w Acr	81.3 kPa	-	71.08 Acr	-	6.3 kJ/m ²
	85% w Acr	62.0 kPa		216.1 2 Alg		8.7 kJ/m ²
	90% w Acr	46.5 kPa		85- 100 g/mol		7.3 kJ/m ²
Chitosan [79]	2% w/v	11.4 MPa	-	3800- 20000 Da	-	1720 J/m ³
Chitosan/fibrin [79]	-	59 MPa		-		1050 J/m ³
chitosan hydrogel / Swollen [80]	-	18.7 kPa	-	61200 0 Da	-	630 kJ/m ³
chitosan hydrogel / Unswollen [80]		23.6 kPa				5460 kJ/m ³

Gel	Solid content	E	Crosslink density	M_w	M_c (b/t crosslinks) g/mol	Toughness
alginate GA [81]	2% w/w + ADD CrossLinker	8.5 kPa	0.05 M	26910	5640	6.5 J/m ²
		16.8 kPa	0.1 M		2970	4.6 J/m ²
		44 kPa	0.15 M		1110	1.85 J/m ²
alginate GA [81]	2% w/w + Ca ²⁺ CL	7.25 kPa	0.24 M	0 g/mol	4380	49.18 J/m ²
		27 kPa	0.3 M		1608	230.2 J/m ²
		58.9 kPa	0.6 M		-	262.65 J/m ²
alginate MA [81]	2% w/w + Ca ²⁺ CL	1 kPa	0.24 M	28000 0 g/mol	35649	6.5 J/m ²
		3.35 kPa	0.3 M		13249	25 J/m ²
		1.28 kPa	0.6 M		-	90.95 J/m ²

Chen et al [82] introduced a linear correlation between concentration of hybrid double-network gels of agar/polyacrylamide (Agar/PAAm) and its toughness/stiffness [82]. This specific hybrid gel can be used to estimate the material properties of the NPC gel, since it is similar to the NPC gel in two ways. First, the concentration of the FG-domains in the NPC central channel is in the same range of the tested gel in Chen's study. Second, estimating Young's modulus of the NPC gel using the correlation for the hybrid gel, results in values of stiffness (elastic modulus) comparable to those measured for a real NPC in-vitro (See next section for the details).

Based on the graph shown in figure 4-6, there is a linear correlation between the concentration of the gel and its mechanical properties. Reading the data point on the red curve,

the gel toughness can be estimated using $T = 31.14C + 249.7$ with $R^2 = .99$; where T is the toughness of the gel (J/m^2) and C is the concentration of the gel (mg/ml). Note that these values were measured by a tearing test on the gel samples, and thus correspond with the mode I toughness value (J_{IC}). However, for the case of the flat end punch, the gel will experience mode II fracture. Therefore, the mode II toughness J_{IIC} remains to be estimated, and we will return to this below. On the other hand, reading the data points of the blue curve will give us a correlation between elastic modulus of the gel and its concentration: $E = 11.93C - 47.01$ with $R^2 = .99$; where E is the Young's modulus of the gel (kPa). So knowing the concentration of FG-domains in the NPC central channel will allow us to estimate the toughness and stiffness values of the gel.

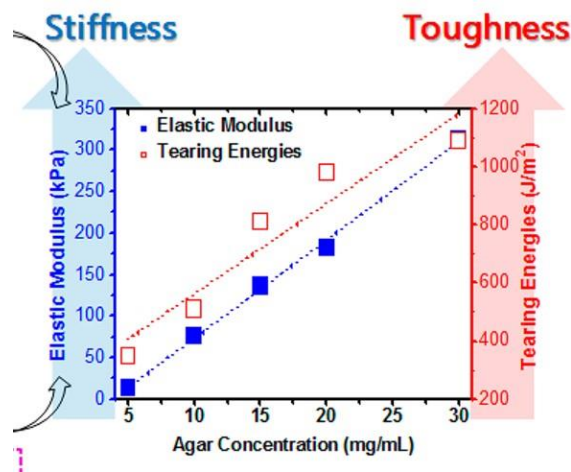


Figure 4-6 The correlation between the gel concentration and elastic modulus (Blue line) and gel concentration and its toughness (red line), reprinted from [82] © 2015 American Chemical Society.

The concentration of the FG-domains in the central channel of the NPC can be calculated in 2 ways:

1. Calculating the fraction of the FG-regions of the nups making the central channel of the NPC (that is to assume the FG-regions of the other nups in the NPC do not contribute to the

gel formation and permeability properties of the central channel, and only the 3 nups - nup54, nup58 and nup62 - are making the plug/central channel) (figure 4-8).

NPC central channel, also called the “plug”, consists of 3 different nups [83]:

- 32 molecules of Nup58 (MW 60,897 KDa)
- 64 molecules of Nup54 (MW 55,435 KDa)
- 128 molecules of Nup62 (MW 53,255 KDa)

Together these 3 nups amount to 12.3 MDa or as measured by Reichelt et al, using scanning transmission electron microscopy, 12 MDa [84].

Each of these 3 nups has different number of residues and different concentration of the FG/FG-like domains per 100 residues. The numbers of the FG/FG domain containing residues are given in the table below extracted from [85]. Based on these numbers (extracted from figure 4-7) the concentration of FG/FG-like domains can be calculated as:

- 128 molecules of nup62, each containing 350 residues with 3.1 FG dipeptides per 100 residues
- 64 molecules of nup54, each containing 92 residues with 10.7 FG dipeptides per 100 residues and 137 residues with 7.3 FG & FG-like dipeptides per 100 residues
- 32 molecules of nup58, each containing 157 residues with 6.9 FG dipeptides per 100 residues and 344 residues with 3.2 FG & FG-like dipeptides per 100 residues

Repeat domain	Residues	FG dipeptides per 100 residues
---------------	----------	--------------------------------

X./.	Nup62	FG	2-352	3.1
X./.	Nup58	FG	2-72, 511-598	6.9
		FG&FG-like	2-259, 511-598	3.2
X./.	Nup54	FG	2-94	10.7
		FG&FG-like	2-139	7.3

Figure 4-7 Number of the residues of the 3 main nups in the NPC central channel and number of FG-repeats per 100 residues [85].

This will result in a total number of FG dipeptides in the central channel of NPC:

$$(128 \times 350 \times 3.1 + 32(157 \times 6.9 + 344 \times 3.2) + 64(92 \times 10.7 + 137 \times 7.3)) / 100 = 3357.8$$

with each FG-dipeptide being 151.16 g/mol [83]:

$$3357.8(\text{FG_Dipeptides}) \times \frac{151.16(\text{g/mol})}{6.022E23(\text{Dipeptides/mol})} = 84.3E-17\text{mg}$$

Next, we calculate the volume of the FG gel located inside the plug or the central channel of the NPC with a diameter of 40-75 nm and length of 40-90 nm [46, 47].

$$V_{\text{plug}} = \pi \left(\frac{40}{2}\right)^2 40(\text{nm}^3) = 50.256E-18\text{ml}$$

This will result in a total concentration of $\frac{84.3E-17(\text{mgFG})}{50.256E-18(\text{mlGel})} = 16.8(\text{mg/ml})$

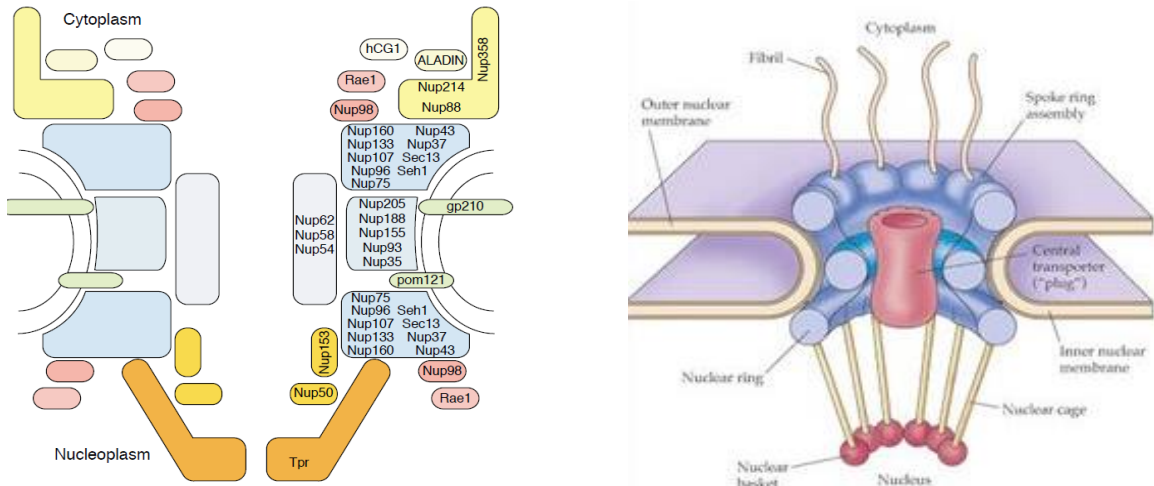


Figure 4-8 a) 3D simplified and non-exhaustive schematic diagram of nucleoporin localization within the metazoan NPC (printed from [86] © 2005 Elsevier Ltd) b) Model of the nuclear pore complex: The complex consists of an assembly of eight spokes attached to rings on the cytoplasmic and nuclear sides of the nuclear envelope [87] © Dr. G. R. Kantharaj.

2. Accounting for the mass fraction of the total FG and FG-like domains in the NPC, assuming that they all contribute in the gel formation process, and that they are uniformly distributed in the NPC which based on Labokha's study [85] is a reasonable assumption.

In their recent study, Labokha et al, [85] characterized the FG domains and FG-like domains⁷ of nups from *Xenopus* for their cohesiveness and hydrogel forming and selectivity properties. Testing gel formation and permeation of the hydrogel generated by dissolving 200 mg/ml of different types of nups in aqueous buffer, they concluded that all of the FG motifs are cohesive and capable of forming a selective hydrogel and together they account for ~1/7 of the attributable mass of NPC proper (120 MDa) [85]. This can be extended to the nups in the central

⁷ Those represent low complexity sequences related to the FG domains but still contain few or no FG motifs in them.

channel as well (with the uniformly distribution assumption) which means $\sim 1/7$ of the total mass of nup54, nup 58 and nup62 (12MDa) or 1.7 MDa.

Similar to previous calculation, using the volume of the central channel the density of of FG-repeats in in the central channel can be calculated as below:

$$1.7MDa = 1.7E6 \times 1.66E-27kg = 2.8E-15mg$$

$$Density = \frac{2.8E-15(mg)}{50.25E-18(ml)} = 55.7(mg / ml)$$

These two estimations are on the same order of magnitude. They differ by a factor of about 3 because of accounting for the globular FG regions of the nups in the second method. Since only unfolded FG-region of the nups are known to contribute in the gel properties and barrier formation in the NPC channel, the value obtained by the first method is slightly preferred over the second one. . The calculated FG concentration from the first method is in the range where the correlation is valid for the hybrid gel used as reference here. The second method produces a value out of the range, and so we use the first value to continue our estimation of mechanical properties.

In Fig. 2-7, the concentration of 16.8 mg/ml corresponds to a toughness of $J = 772.9 \text{ j/m}^2$ and elastic modulus of $E = 153.4 \text{ kPa}$. The value of Young's modulus estimated by the hybrid gel correlation agrees very well with those measured for NPC gel in-vitro: AFM force-indentation studies on a real NPC reported a value of $E = 0.15 \text{ [70] - 1 MPa [69]}$ for this gel. Therefore one can conclude the hybrid gel has enough similarities to the NPC gel and the estimated values are reasonable.

The Young's modulus of 0.15 MPa assuming an incompressible gel material ($\nu=0.5$) will give a shear modulus of $\mu=0.05$ Mpa⁸. So comparing the J and μ values used in Shergold and Fleck's model (table 4-2), the ratios between the toughness and shear modulus are comparable and are of the same order of magnitude. So it is only baculovirus size (R) in our case which makes the $J/\mu R$ ratio so large in our case.

Table 4-2 Toughness and shear modulus values for rubber, human skin and NPC gel.

Material	J_{IC} (kJ/m ²)	μ (MPa)
silicon rubber (452) [64]	3.8	0.4
human skin [64]	2.5	0.1
NPC gel (estimated from Agar correlations)	0.77	0.05

Note the estimated value for toughness of the gel is the mode I fracture toughness (Plane strain fracture when a normal load is applied to the flat surface). For the flat-ended punch penetrating into the soft gel, the mode II of fracture happens, therefore another step is required to estimate J_{II_C} . For this purpose, the correlation between the two modes of the fracture toughness for polymer matrix can be estimated by:

$$J_{I_C} = \frac{K_{I_C}^2(1-\nu^2)}{E}, J_{II_C} = \frac{K_{II_C}^2(1-\nu^2)}{E} \quad \text{Eq 4-19}$$

Where K_{I_C} and K_{II_C} are mode I and II stress intensity factors [88] and the correlation between them is determined on the basis of experimental data for different materials. The K_{II_C} / K_{I_C} ratio varies from 0.75 to 1.29 which is material dependent but specimen geometry and test procedure independent. This ratio for the only polymeric material studied for the mixed mode of

⁸ $\mu = \frac{E}{2(1+\nu)}$

fracture is 0.89 [89]. Therefore taking this ratio along with the correlation given by *Jamali* [88] for the toughness values, J_{II_C} is estimated as:

$$\frac{J_{II_C}}{J_{I_C}} = \left(\frac{K_{II_C}}{K_{I_C}}\right)^2 = 0.89^2 \text{ So, } J_{II_C} = 612.21 \text{ J/m}^2$$

4.3.3 Strain hardening exponent of the NPC gel

To the best of our knowledge, no such study has been done on the NPC or any in-vitro equivalent of FG- hydrogel specifically focusing on the mechanical properties and strain hardening behavior of the hyperelastic gel. The only mechanical investigation of NPC is an AFM force-indentation measurement by *Liashkhovich et al*, where the deformation of nuclear basket of NPC was measured under several different values of force [47]. From those data one can simply calculate the stress strain values corresponding to each force level and by fitting the stress-strain relationship of Ogden hyperelastic material ($\sigma = K\varepsilon^\alpha$ where K is the material strength/Young's modulus) the strain hardening exponent can be approximated. However, these measurements are done on the nuclear side of the nuclear envelope and are properties of the nuclear basket not the gel inside the NPC central channel.

For lack of solid data, we have decided to treat the strain hardening exponent as a free parameter in our model. The mechanical model presented above was tested for several different strain-hardening values for the flat model ($\alpha=2,3,4$) and for the case of the sharp punch the model is tested with $\alpha=3$.

In order to investigate the contribution of each force in the total force required for penetration of the virus inside the NPC gel, the equations in each part of the model are solved simultaneously with the physical properties of the baculovirus and NPC gel. Table 4-3 summarizes all the model parameters for virus penetration in NPC gel.

Table 4-3 Summary of the parameters of the soft solid penetration model

Gel parameters	Value
Mode I fracture toughness (J_{IC})	0.7 (kJ/m ²)
Mode II fracture toughness (J_{IIC})	0.5 (kJ/m ²)
Shear modulus (μ)	0.05 (MPa)
Strain hardening coefficient (α)	varying
Virus parameters	
Radius at tip (R_b)	3.8 (nm)
Radius at stem (R_t)	15 (nm)
Length (nm)	250-300 nm

4.4 Flat-ended model predictions

4.4.1 Blunt conical tip baculovirus

As mentioned earlier, the model was given freedom on the value of strain-hardening parameter due to the lack of experimental measurement of the value for NPC gel. Here several cases with different α values are evaluated. Table 4-4 summarizes the total force values required for penetration of the flat-ended punch into the NPC gel.

Table 4-4 Punching force of the flat-ended model for different α values

Strain-hardening value	Total force required (pN)
2	3.17E4
3	5.54E4
4	2.57E6

Notice for all of these cases with the estimated toughness value, the force is much higher than the force that can be provided by actin polymerization in the wake of at baculovirus.

Besides, for all these cases, the concept of having an initial crack of radius b that enclose a cylindrical material that is compressed longitudinally and expanded radially to accommodate the punch is inapplicable. In the model b is to be optimized for the contribution of the 4 different terms of the model so that the total punching force required is minimized. However, for these cases listed above the optimized value of the b is extremely low (as low as 0.01 nm). This implies that the initial crack cannot exist or that the continuum model does not apply. Therefore we test a modified version of the model in which we neglect the existence of the initial crack of length b to be expanded and compressed.

Before moving on to that modified version of the model, we would like to know if for any set of parameters we can get total punching forces on the same order of magnitude as the actin polymerization force. Therefore, in the following subsections we are going to manipulate the parameters values and evaluate the model to see if the force value shows any significant changes. Studying the contribution of the 4 different terms of the model, it is clear that the total force value is dominated by the crack formation energy and the other 3 terms are on the order of several pN. Therefore, we can conclude the toughness value is the most important parameter in the model, so the model is evaluated for different toughness values and the contribution of each force term is tracked.

1. For the first case, we set $\alpha=3$ and test the model for different toughness values. Table 4-5 summarizes the contribution of each term in the total force for different values of toughness. Note that in the table the column b_{min} shows the optimized value of the initial crack length to have the minimum total force. For first 3 cases in the table, the idea of the minimized force is not applicable since the optimized b value will have extremely small values (<0.01 nm) which is not possible physically.

Note that, even for very small values of toughness ($J \sim 0.02 \text{ mJ/m}^2$), the contribution of the tip of the virus is still much higher and does not match our expectations for the actin polymerization force. We also noticed that the total punching force decreases with decreasing toughness. However the crack formation force and the force required for the entrance of the tip decrease more significantly. For the last case of very low toughness value, the tip term increases again which is due to the different contributions of b and J . To explain this observation, one should notice the effect of the toughness value on each term as well as its effect on the optimal value of b for which the required force is minimal. As predicted by Shergold and Fleck [64], lower values of toughness will result in larger optimal b values (see figure 4-2) and the larger b value affects the total force. For the last case, the contribution of b -containing terms becomes more dominant compared to crack formation force and the total punching force increases again.

Table 4-5 Force values for the case study of $\alpha=3$ and different toughness values

Case	J (j/m^2)	Crack formation (pn)	Column compression (pn)	Hole expansion (pn)	Tip term (pn)	Total force (pn)	b_{\min} (nm)
1-1	500	3.1E4	383.1	383.6	2.3E4	5.6E4	0.01
1-2	200	1.3E4	383.1	383.6	2.3E4	3.6E4	0.01
1-3	20	1.3E3	383.1	383.6	2.3E4	2.5E4	0.01
1-4	2	377	127.7	128.2	7.7E3	8.4E3	0.03
1-5	0.2	100.6	47.9	48.3	2.9E3	3.1E3	0.08
1-6	0.02	31.6	15.4	16.7	938	1E3	0.25
1-7	0.002	9.8	5.3	5.2	327.4	347.7	0.75
1-8	2E-4	3	2.2	1.8	168	175.1	1.85
1-9	2E-5	1.2	1	0.5	222.6	225.2	3.1

2. For the second case study, we set $\alpha=4$ and test the model with different toughness values.

Table 4-6 summarizes the contribution of each term in the total force for different values of toughness. The column b_{min} shows the optimized value of the initial crack length to have the minimum total force. In this case we can see that the minimal b value has a meaningful value, however the total force values are still much higher than the expected value and similar to case one, there is a lower limit for the decreased value of the toughness, after which the required force still increases.

Table 4-6 Force values for the case study of $\alpha=4$ and different toughness values

Case	J (j/m ²)	Crack formation (pn)	Column compression (pn)	Hole expansion (pn)	Tip term (pn)	Total force (pn)	b_{min} (nm)
2-1	500	6.3E4	2E4	1E4	2.5E6	2.6E6	0.02
2-2	200	3.8E4	9.1E3	4.6E3	1.1E6	1.2E6	0.03
2-3	20	7.5E3	2.13E3	1.1E3	2.8E5	2.9E5	0.06
2-4	2	1.6E3	485	246	5.9E4	6.1E4	0.13
2-5	0.2	341	112.9	59.2	1.4E4	1.4E4	0.27
2-6	0.02	73.3	25.8	14.7	3.2E3	3.3E3	0.57
2-7	0.002	16.1	6.6	4.4	854.9	882	1.16
2-8	2E-4	3.8	2.3	1.5	363.9	371.6	2.11
2-9	2E-5	1.2	0.9	0.5	377.5	380	3.11

3. For this case, we set $\alpha=2$ and test the model with different toughness values. Table 4-7 summarizes the contribution of each term in the total force for different values of toughness. Like before, the column b_{min} shows the optimized value of the initial crack length to have the minimum total force. In this case again there is no meaningful crack length for high toughness values. Besides, the total force values are still much higher than

the expected value and similar to case one, and only in the case 3-8 where toughness is $J=0.2 \text{ mJ/m}^3$ the punching force is on the order of 100 pN and close to the actin polymerization force.

Table 4-7 Force values for the case study of $\alpha=2$ and different toughness values

Case	J (j/m^2)	Crack formation (pn)	Column compression (pn)	Hole expansion (pn)	Tip term (pn)	Total force (pn)	b_{\min} (nm)
3-1	500	3.1E4	2.3	13.5	245	3.2E4	0.01
3-2	200	1.3E4	2.3	13.5	245	1.3E4	0.01
3-3	20	1.3E3	2.3	13.5	245	1.5E3	0.01
3-4	2	125.7	2.3	13.5	245	386.4	0.01
3-5	0.2	12.6	2.3	13.5	245	273.3	0.01
3-6	0.02	2.5	2.3	11.9	222.1	238.8	0.02
3-7	0.002	2.3	2.3	6.9	149.7	161.2	0.18
3-8	2E-4	2	2.1	2.3	93.9	100.3	1.39
3-9	2E-5	1.2	1	0.5	159	161.7	3.4

So, as shown in these 3 cases, for most of the toughness values the idea of the initial crack of length b is not applicable. Therefore, we need to modify our model. The modified model is presented in section 4.2.2 and its predictions are discussed below.

4.4.2 Blunt conical tip baculovirus – modified model

Here again, for several values of the strain-hardening coefficient, we estimated the total force for punch the blunt conical tip virus into the NPC gel. The total required force is $1.2E7 \text{ pN}$ for the 3 choices of α and it can be seen that in this case change of α only affects the tip term contribution (by several pN) which compared to the crack formation is negligible. In this case, similar to the previous model, the high toughness value means a punching force that is much

higher than actin polymerization force. This implies that purely mechanical penetration of the virus into the gel is unlikely.

For this model, the contribution of the terms and the change of crack formation force with the toughness value are tracked to see what parameter values could lower the required force to the level of the actin polymerization force. Table 4-8 lists the values of the punching force for different toughness values. As it can be seen in the table below, the toughness affects the crack formation force; only for very low value of gel toughness (e.g. 0.2 mJ/m³) does the punching force become low enough to allow the mechanical breakthrough using the actin polymerization force. In other words, the toughness values needs to be very small to have forces in the order of hundreds of pN.

Table 4-8 Force values for the case study of $\alpha=3$ and different toughness values

Case	J (j/m ²)	Crack formation (pn)	Fourth term (pn)	total force (pN)
4-1	500	1.2E7	58.7	1.2E7
4-2	200	4.77E6	58.7	4.8E6
4-3	20	4.77E5	58.7	4.8E5
4-4	2	4.77E4	58.7	4.78E4
4-5	0.2	4.77E3	58.7	4.83E3
4-6	0.02	477.5	58.7	536.2
4-7	2E-3	47.75	58.7	106.43
4-8	2E-4	4.8	58.7	63.5
4-9	2E-5	0.5	58.7	59.2

4.4.3 Sharp conical tip baculovirus

This force value will depend on the depth of the penetration at the tip. By using the mechanical properties (e.g. toughness, shear modulus and strain hardening coefficient) obtained in previous sections the total load required is estimated: For this model, we only use one strain-hardening value $\alpha=3$ and the rest of the parameters for the model are the same as what listed in table 4-3. Evaluating the sharp-ended model, the total force required for penetration of the sharp punch into the gel of toughness 770 J/m^3 is $9\text{E}4 \text{ pN}$, which is still much higher than the actin polymerization force. One more time, we manipulated the parameter values for the model to find for which toughness values the force might match the expected values. Table 4-9 lists the contribution of the 2 terms of the sharp model to the total punching force and we can see for small J value (e.g. in the order of mJ/m^3) the force will be the order of hundreds of pN.

Table 4-9 Force values for the sharp model with $\alpha=3$ and different toughness values

Case	$J \text{ (j/m}^2\text{)}$	Crack formation (pn)	Strain energy (pn)	Total force (pn)	$a \text{ (nm)}$
5-1	700	8.4E4	5.9E3	9E4	0.06
5-2	200	2.4E4	5.9E3	3E4	0.06
5-3	20	6.4E3	1.8E3	8.2E3	0.16
5-4	2	1.7E3	451.4	2.3E3	0.46
5-5	0.2	495.4	129	664.5	1.31
5-6	0.02	145.7	44.3	190	3.66
5-7	0.002	41	16	57	10.31
5-8	2E-4	11.6	8	19.6	29.1

For the sharp-ended model, the force values are less comparable to the similar cases of the flat-ended model. This is expected as the sharp tip increases the pressure and enhances the entrance of the punch into the gel. Experimental studies by Shergold [65] and Das [66] also reported higher punching forces for the blunt needle (*i.e.* flat-ended punch).

In summary, for all of the models, the gel must have very low toughness values to be penetrable by the baculovirus if the latter is solely driven by actin polymerization. Table 4-10 lists the force values for the toughness values tested in each model. The findings of the deep penetration models suggest that the actin polymerization force would not be sufficient for purely mechanical entry of the virus into the NPC gel, and there might be another biochemical mechanism that facilitates the entrance of the virus.

Table 4-10 The total punching force (pN) predicted by each model for $\alpha=3$ for different toughness values

Toughness	Flat end model	Flat end modified model	Sharp-ended model
700	5.6E4	1.2E7	9E4
200	3.6E4	4.8E6	3E4
20	2.5E4	4.8E5	8.2E3
2	8.4E3	4.78E4	2.3E3
0.2	3.1E3	4.83E3	664.5
0.02	1E3	536.2	190
0.002	347.7	106.43	57
2E-4	175.1	63.5	19.6

Chapter 5: Conclusion

In this chapter, I summarize the major findings and contributions of my research. I also list limitations of my current work and give recommendations for future work.

5.1 Baculovirus nucleocapsid rides on the actin tail

Baculovirus nucleocapsid is able to transduce a wide range of mammalian cells without cytotoxic effects [90, 91], and is one of the best candidates for viral vector-based gene therapy application [92-94]. Therefore studying the mechanism of baculovirus infection and how it is transported inside the host cell has been an interesting topic of research for some years [4]. Several experimental studies focused on the cellular entry and trafficking of the baculovirus and some others tried to investigate its nucleus entry.

The mechanism by which baculovirus transfers its genome to the nucleus of the host cell is an understudied topic. Inspired by the experimental observation of Au *et al.* [3, 5, 95], in this study we investigated the hypothesis of mechanical entry to the nucleus. In their study Au *et al.*, investigated viral and cellular proteins involved in the process and examined the nuclear import mechanism of the rod-shaped nucleocapsid of the virus and showed they are imported to the nucleus through NPCs [4]. Through a series of investigations they proved the followings: 1) Baculovirus nuclear import is an unconventional nuclear mechanism which does not require an energy regenerating source. 2) Nuclear entry of the baculovirus is not due to disruption of the nuclear envelope. 3) Inhibition of receptor-mediated nuclear entry does not affect efficiency of nuclear import. 4) GTP hydrolysis which is the energy source for NTR/NLS import is not required for nucleocapsid import. 5) Intact F-actin is necessary for nuclear import of the viral nucleocapsid and 6) Inhibiting activation of the Arp2/3 complex impedes nuclear entry of the virus. With these findings, they suggested that actin nucleation and polymerization are not only

required for the intracellular trafficking of the virus but also for its NPC translocation. This has motivated the idea of mechanical breakthrough in which actin polymerization and Arp2/3 proteins are the major contributor [4].

Here, using a microscopic approach and focusing on the dynamics of the actin polymerization, we developed a mathematical model to describe the physical behavior and force velocity profile of the virus riding on the actin comet tail. The model uses actin monomer concentration, virus size and filament properties, and predicts a biphasic force velocity relation with rapidly decreasing velocity in small external forces, followed by a more slowly decreasing velocity for larger forces. This predicts a steady state velocity of 230 nm/s and a stall force of ~ 50 pN for baculovirus. This force value is a key factor for testing the hypothesis of the purely mechanical entry of the virus to the nucleus.

5.2 Baculovirus entry into NPC

Our results of modeling the NPC gel as a continuum hydrogel punctured by the baculovirus shows that the entry of the baculovirus to NPC may not be a purely mechanical event. Comparing the force generated by actin polymerization and that required for breakthrough into the NPC gel, we find that the NPC gel needs to be very soft with a toughness value of ~ 2 mJ/m³, which is orders of magnitude below estimated values. The lowest toughness value for *in vitro* gels that are comparable with NPC in some sense is ~ 2 J/m³. Depending on their concentration and chain length, *in vitro* gels have toughness values ranging from 10s J/m³ to 10s kJ/m³. Those having toughness value lower than this lower bound likely have insufficient concentration of the polymer in the gel and may not show the selective permeability properties [54].

Since there is no direct study on the mechanical properties of the NPC central channel, we tested the model for several different values of the strain hardening exponents of the NPC gel for the case of flat-bottomed punch, to see if in any case the required punching force would fall into our expected force limit. This parameter manipulation shows significant changes in force values predicted by the flat model.

Therefore, based on our model predictions, in order for the actin polymerization force to cause entry through the NPC, the gel inside the central channel of NPC has to be very soft. The strain-hardening parameter α is not a very important parameter in our story. By varying α between 2 and 4, we are unable to lower the required force much if the realistic J value is used; therefore, the key parameter is J . These results do not support the hypothesis of the purely mechanical puncture of the NPC gel by baculovirus.

5.3 Concluding remarks and future work

Although our results cast doubt on the hypothesis of a purely mechanical entry of the baculovirus into the NPC driven by actin polymerization, we should not dismiss the possibility of NPC using several different modes of translocations for different cargos. It is also possible that through some unknown biochemical interactions, as soon as the conical tip of the virus get entangled into the cytoplasmic filaments of the NPC, the FG corona surrounding the cytoplasmic entrance retracts and opens up the hole to admit the baculovirus.

There are several limitations in our model that cast some doubts on the results. For example for the actin force estimation, experimental evidences of baculovirus pushing into the NE suggest much higher force that can indeed bend the NE. This might be due to the fact that many of the actin polymerization parameters were estimated based on the cytoplasmic values,

whereas the rates and concentrations near the surface of the virus might be different from those observed in the cytoplasm. Knowing the exact value of these parameters, we can later refine the model to predict more precise results. Besides, there is a possibility of the invalid parameter estimation for capping and dissociation rate of the actin filaments. Due to the lack of experimental data, we estimated these values in a way to best match the experimental observations.

In the second part there are several limitations as well. First of all, the (continuum) hydrogel model is used to represent the NPC central channel, which is only a first attempt to study this nuclear import phenomenon. Maybe other NPC models such as polymer brush would give more reasonable predictions of this entry process. We should not dismiss the fact that the interaction of the FG-nups at the molecular level and the suggested configuration and chain entanglement in the polymer brush might be a major role player in estimation of the force. Besides, it is also possible that the details of the mechanical model are incorrect for the case of baculovirus nucleocapsid entry to the NPC. Another limitation is regarding the parameter estimation. Due to the lack of experimental evidences we approximated the value of the gel toughness and arbitrarily chosen the value of the strain hardening coefficient. For the toughness estimation, we estimated the value with the *in vitro* gel (agarose). However, we need to mention that the mechanical properties of the agarose gel have been measured in room temperature and toughness and Young's modulus values might be different in physiologic temperatures. Also it is possible that due to the very small size of the NPC gel, the mechanical behavior of the soft gel is much different from those observed in macroscale. Another limitation in this model is the simplified treatments of the geometry of the entry process, i.e. penetration into an infinite sheet of the gel without the constraints from the boundary conditions. Given the fact that the depth of

the nuclear pore is comparable with its diameter and the size of the baculovirus, the penetration model through an infinite gel may be inappropriate. Therefore, although our results do not seem to directly support the hypothesis of a purely mechanical entry, they have not disproved the hypothesis either. The factors enumerated in the above are other possible explanations for the discrepancy.

Although this work provides some insight to the baculovirus nuclear import mechanism, there are still several questions to be addressed in the future studies. For example, our results suggested that this entry may not be a purely mechanical one. But this does not mean that the actin force and mechanical aspect cannot have a role in the nuclear import. However, those additional factors and how they affect viral entry are currently unknown. Characterization of this mechanism will be crucial to develop more efficient ways of baculovirus import into the host nucleus.

Another future area of research could be experimental study on the mechanical properties of the NPC gel. Such observations and measurements will provide firmer basis for our proposed values for the gel toughness and strain hardening. That will give researcher more insight on this entry mechanism and will help determining the contribution of actin polymerization in this semi-mechanical entry.

Bibliography

1. Ohkawa, T., L.E. Volkman, and M.D. Welch, *Actin-based motility drives baculovirus transit to the nucleus and cell surface*. The Journal of cell biology, 2010. **190**(2): p. 187-195.
2. Welch, M.D. and M. Way, *Arp2/3-mediated actin-based motility: a tail of pathogen abuse*. Cell host & microbe, 2013. **14**(3): p. 242-255.
3. Au, S. and N. Panté, *Nuclear transport of baculovirus: revealing the nuclear pore complex passage*. Journal of structural biology, 2012. **177**(1): p. 90-98.
4. Au, S., *Nuclear import of baculovirus autographa californica multiple nucleopolyhedrovirus (AcMNPV)*. 2013, University of British Columbia.
5. Au, S., W. Wu, and N. Panté, *Baculovirus nuclear import: open, nuclear pore complex (NPC) sesame*. Viruses, 2013. **5**(7): p. 1885-1900.
6. Rohrmann, G.F., *Baculovirus molecular biology*. 2013.
7. Cheshenko, N., et al., *A novel system for the production of fully deleted adenovirus vectors that does not require helper adenovirus*. Gene therapy, 2001. **8**(11): p. 846-854.
8. Airene, K.J., et al., *Baculovirus: an insect-derived vector for diverse gene transfer applications*. Molecular Therapy, 2013. **21**(4): p. 739-749.
9. Dickinson, R.B., *Models for actin polymerization motors*. Journal of mathematical biology, 2009. **58**(1-2): p. 81-103.
10. Pollard, T.D. and G.G. Borisy, *Cellular motility driven by assembly and disassembly of actin filaments*. Cell, 2003. **112**(4): p. 453-465.
11. Mullins, R.D., J.A. Heuser, and T.D. Pollard, *The interaction of Arp2/3 complex with actin: nucleation, high affinity pointed end capping, and formation of branching networks of filaments*. Proceedings of the National Academy of Sciences, 1998. **95**(11): p. 6181-6186.
12. Cooper, G.M. and R.E. Hausman, *The cell*. 2000: Sinauer Associates Sunderland.
13. Prost, J., et al., *The physics of Listeria propulsion*, in *Cell Motility*. 2008, Springer. p. 1-30.
14. Upadhyaya, A., et al., *Probing polymerization forces by using actin-propelled lipid vesicles*. Proceedings of the National Academy of Sciences, 2003. **100**(8): p. 4521-4526.
15. Giardini, P.A., D.A. Fletcher, and J.A. Theriot, *Compression forces generated by actin comet tails on lipid vesicles*. Proceedings of the National Academy of Sciences, 2003. **100**(11): p. 6493-6498.
16. Zhu, J., *Force generation by actin polymerization: Nanoscale to microscale*. 2008: ProQuest.
17. Peskin, C.S., G.M. Odell, and G.F. Oster, *Cellular motions and thermal fluctuations: the Brownian ratchet*. Biophysical journal, 1993. **65**(1): p. 316.
18. Mogilner, A., *Mathematics of cell motility: have we got its number?* Journal of mathematical biology, 2009. **58**(1-2): p. 105-134.
19. Marcy, Y., et al., *Forces generated during actin-based propulsion: a direct measurement by micromanipulation*. Proceedings of the National academy of Sciences of the United States of America, 2004. **101**(16): p. 5992-5997.
20. Gerbal, F., et al., *An elastic analysis of Listeria monocytogenes propulsion*. Biophysical journal, 2000. **79**(5): p. 2259-2275.

21. Flyvbjerg, H., et al., *Physics of Bio-Molecules and Cells: Les Houches Session LXXV, 2-27 July 2001*. Vol. 75. 2003: Springer Science & Business Media.
22. Mogilner, A. and G. Oster, *Cell motility driven by actin polymerization*. Biophysical journal, 1996. **71**(6): p. 3030.
23. Mogilner, A. and G. Oster, *Force generation by actin polymerization II: the elastic ratchet and tethered filaments*. Biophysical journal, 2003. **84**(3): p. 1591-1605.
24. Cameron, L.A., et al., *Dendritic organization of actin comet tails*. Current Biology, 2001. **11**(2): p. 130-135.
25. Wiesner, S., et al., *A biomimetic motility assay provides insight into the mechanism of actin-based motility*. The Journal of cell biology, 2003. **160**(3): p. 387-398.
26. Dickinson, R.B. and D.L. Purich, *Clamped-filament elongation model for actin-based motors*. Biophysical journal, 2002. **82**(2): p. 605-617.
27. Dickinson, R.B., L. Caro, and D.L. Purich, *Force generation by cytoskeletal filament end-tracking proteins*. Biophysical journal, 2004. **87**(4): p. 2838-2854.
28. Parekh, S.H., et al., *Loading history determines the velocity of actin-network growth*. Nature cell biology, 2005. **7**(12): p. 1219-1223.
29. Carlsson, A.E., *Growth of branched actin networks against obstacles*. Biophysical journal, 2001. **81**(4): p. 1907-1923.
30. Carlsson, A., *Growth velocities of branched actin networks*. Biophysical journal, 2003. **84**(5): p. 2907-2918.
31. Mueller, J., et al., *Electron tomography and simulation of baculovirus actin comet tails support a tethered filament model of pathogen propulsion*. PLoS biology, 2014. **12**(1): p. e1001765.
32. Zhu, J. and A. Mogilner, *Mesosopic model of actin-based propulsion*. PLoS computational biology, 2012. **8**(11): p. e1002764.
33. Schreiber, C.H., M. Stewart, and T. Duke, *Simulation of cell motility that reproduces the force-velocity relationship*. Proceedings of the National Academy of Sciences, 2010. **107**(20): p. 9141-9146.
34. Lee, K.-C. and A.J. Liu, *Force-velocity relation for actin-polymerization-driven motility from Brownian dynamics simulations*. Biophysical journal, 2009. **97**(5): p. 1295-1304.
35. McGrath, J.L., et al., *The force-velocity relationship for the actin-based motility of *Listeria monocytogenes**. Current Biology, 2003. **13**(4): p. 329-332.
36. Heinemann, F., H. Doschke, and M. Radmacher, *Keratocyte lamellipodial protrusion is characterized by a concave force-velocity relation*. Biophysical journal, 2011. **100**(6): p. 1420-1427.
37. Prass, M., et al., *Direct measurement of the lamellipodial protrusive force in a migrating cell*. The Journal of cell biology, 2006. **174**(6): p. 767-772.
38. Zimmermann, J., et al., *Actin filament elasticity and retrograde flow shape the force-velocity relation of motile cells*. Biophysical journal, 2012. **102**(2): p. 287-295.
39. Tran, E.J. and S.R. Wentz, *Dynamic nuclear pore complexes: life on the edge*. Cell, 2006. **125**(6): p. 1041-1053.
40. Cronshaw, J.M., et al., *Proteomic analysis of the mammalian nuclear pore complex*. The Journal of cell biology, 2002. **158**(5): p. 915-927.

41. Floch, A.G., B. Palancade, and V. Doye, *Fifty years of nuclear pores and nucleocytoplasmic transport studies: multiple tools revealing complex rules*. *Methods in cell biology*, 2013. **122**: p. 1-40.
42. Beck, M., et al., *Nuclear pore complex structure and dynamics revealed by cryoelectron tomography*. *Science*, 2004. **306**(5700): p. 1387-1390.
43. Stoffler, D., et al., *Cryo-electron tomography provides novel insights into nuclear pore architecture: implications for nucleocytoplasmic transport*. *Journal of molecular biology*, 2003. **328**(1): p. 119-130.
44. Lim, R.Y., U. Aebi, and B. Fahrenkrog, *Towards reconciling structure and function in the nuclear pore complex*. *Histochemistry and cell biology*, 2008. **129**(2): p. 105-116.
45. Peters, R., *Translocation through the nuclear pore: Kaps pave the way*. *Bioessays*, 2009. **31**(4): p. 466-477.
46. Panté, N. and M. Kann, *Nuclear pore complex is able to transport macromolecules with diameters of ~ 39 nm*. *Molecular biology of the cell*, 2002. **13**(2): p. 425-434.
47. Liashkovich, I., et al., *Exceptional structural and mechanical flexibility of the nuclear pore complex*. *Journal of cellular physiology*, 2011. **226**(3): p. 675-682.
48. Goryaynov, A.G., *MOLECULAR SIZE AND CHARGE EFFECTS ON NUCLEOCYTOPLASMIC TRANSPORT STUDIED BY SINGLE-MOLECULE MICROSCOPY*. 2013, Bowling Green State University.
49. Patel, S.S., et al., *Natively unfolded nucleoporins gate protein diffusion across the nuclear pore complex*. *Cell*, 2007. **129**(1): p. 83-96.
50. Takeyasu, K., *Atomic Force Microscopy in Nanobiology*. 2014: CRC Press.
51. Wente, S.R. and M.P. Rout, *The nuclear pore complex and nuclear transport*. *Cold Spring Harbor perspectives in biology*, 2010. **2**(10): p. a000562.
52. Lim, R.Y., et al., *Flexible phenylalanine-glycine nucleoporins as entropic barriers to nucleocytoplasmic transport*. *Proceedings of the National Academy of Sciences*, 2006. **103**(25): p. 9512-9517.
53. Lim, R.Y., et al., *Nanomechanical basis of selective gating by the nuclear pore complex*. *Science*, 2007. **318**(5850): p. 640-643.
54. Frey, S., R.P. Richter, and D. Görlich, *FG-rich repeats of nuclear pore proteins form a three-dimensional meshwork with hydrogel-like properties*. *Science*, 2006. **314**(5800): p. 815-817.
55. Frey, S. and D. Görlich, *A saturated FG-repeat hydrogel can reproduce the permeability properties of nuclear pore complexes*. *Cell*, 2007. **130**(3): p. 512-523.
56. Ribbeck, K. and D. Görlich, *Kinetic analysis of translocation through nuclear pore complexes*. *The EMBO journal*, 2001. **20**(6): p. 1320-1330.
57. Frey, S. and D. Görlich, *FG/FxFG as well as GLFG repeats form a selective permeability barrier with self-healing properties*. *The EMBO Journal*, 2009. **28**(17): p. 2554-2567.
58. Yamada, J., et al., *A bimodal distribution of two distinct categories of intrinsically disordered structures with separate functions in FG nucleoporins*. *Molecular & Cellular Proteomics*, 2010. **9**(10): p. 2205-2224.
59. Rout, M.P., et al., *Virtual gating and nuclear transport: the hole picture*. *Trends in cell biology*, 2003. **13**(12): p. 622-628.
60. Ribbeck, K. and D. Görlich, *The permeability barrier of nuclear pore complexes appears to operate via hydrophobic exclusion*. *The EMBO journal*, 2002. **21**(11): p. 2664-2671.

61. Howard, J., *Mechanics of motor proteins and the cytoskeleton*. 2001.
62. Goley, E.D., et al., *Dynamic nuclear actin assembly by Arp2/3 complex and a baculovirus WASP-like protein*. *Science*, 2006. **314**(5798): p. 464-467.
63. Au, S., et al., *A novel mechanism for nuclear import by actin-based propulsion used by the baculovirus nucleocapsid*. *J Cell Sci*, 2016: p. jcs. 191668.
64. Shergold, O.A. and N.A. Fleck. *Mechanisms of deep penetration of soft solids, with application to the injection and wounding of skin*. in *Proceedings of the Royal Society of London A: Mathematical, Physical and Engineering Sciences*. 2004. The Royal Society.
65. Shergold, O.A. and N.A. Fleck, *Experimental investigation into the deep penetration of soft solids by sharp and blunt punches, with application to the piercing of skin*. *Journal of biomechanical engineering*, 2005. **127**(5): p. 838-848.
66. Das, S. and A. Ghatak, *Puncturing of soft gels with multi-tip needles*. *Journal of materials science*, 2011. **46**(9): p. 2895-2904.
67. Cooper, J., et al., *Evaluation of a needle-free injection system for local anaesthesia prior to venous cannulation*. *Anaesthesia*, 2000. **55**(3): p. 247-250.
68. Frick, T., et al., *Resistance forces acting on suture needles*. *Journal of Biomechanics*, 2001. **34**(10): p. 1335-1340.
69. Bestembayeva, A., et al., *Nanoscale stiffness topography reveals structure and mechanics of the transport barrier in intact nuclear pore complexes*. *Nature nanotechnology*, 2015. **10**(1): p. 60-64.
70. Eisele, N.B., et al., *Viscoelasticity of thin biomolecular films: a case study on nucleoporin phenylalanine-glycine repeats grafted to a histidine-tag capturing QCM-D sensor*. *Biomacromolecules*, 2012. **13**(8): p. 2322-2332.
71. DeKosky, B.J., et al., *Hierarchically designed agarose and poly (ethylene glycol) interpenetrating network hydrogels for cartilage tissue engineering*. *Tissue Engineering Part C: Methods*, 2010. **16**(6): p. 1533-1542.
72. Chang, C.-W., et al., *PEG/clay nanocomposite hydrogel: a mechanically robust tissue engineering scaffold*. *Soft Matter*, 2010. **6**(20): p. 5157-5164.
73. Gautreau, Z., *Characterizing viscoelastic properties of polyacrylamide gels*. 2006, Worcester Polytechnic Institute.
74. Shiah, J.-G., et al., *Biodistribution and antitumour efficacy of long-circulating N-(2-hydroxypropyl) methacrylamide copolymer–doxorubicin conjugates in nude mice*. *European Journal of Cancer*, 2001. **37**(1): p. 131-139.
75. Constantinides, G., et al., *Probing mechanical properties of fully hydrated gels and biological tissues*. *Journal of biomechanics*, 2008. **41**(15): p. 3285-3289.
76. Chen, J., et al., *High-toughness polyacrylamide gel containing hydrophobic crosslinking and its double network gel*. *Polymer*, 2016. **87**: p. 73-80.
77. Wang, L., G. Shan, and P. Pan, *Highly enhanced toughness of interpenetrating network hydrogel by incorporating poly (ethylene glycol) in first network*. *RSC Advances*, 2014. **4**(108): p. 63513-63519.
78. Sun, J.-Y., et al., *Highly stretchable and tough hydrogels*. *Nature*, 2012. **489**(7414): p. 133-136.
79. Fernandez, J.G. and D.E. Ingber, *Unexpected strength and toughness in chitosan-fibroin laminates inspired by insect cuticle*. *Advanced materials*, 2012. **24**(4): p. 480-484.

80. Wang, T., M. Turhan, and S. Gunasekaran, *Selected properties of pH-sensitive, biodegradable chitosan–poly (vinyl alcohol) hydrogel*. *Polymer International*, 2004. **53**(7): p. 911-918.
81. Kong, H.J., E. Wong, and D.J. Mooney, *Independent control of rigidity and toughness of polymeric hydrogels*. *Macromolecules*, 2003. **36**(12): p. 4582-4588.
82. Chen, Q., et al., *Simultaneous enhancement of stiffness and toughness in hybrid double-network hydrogels via the first, physically linked network*. *Macromolecules*, 2015. **48**(21): p. 8003-8010.
83. Solmaz, S.R., et al., *Molecular architecture of the transport channel of the nuclear pore complex*. *Cell*, 2011. **147**(3): p. 590-602.
84. Reichelt, R., et al., *Correlation between structure and mass distribution of the nuclear pore complex and of distinct pore complex components*. *The Journal of Cell Biology*, 1990. **110**(4): p. 883-894.
85. Labokha, A.A., et al., *Systematic analysis of barrier-forming FG hydrogels from *Xenopus* nuclear pore complexes*. *The EMBO journal*, 2013. **32**(2): p. 204-218.
86. Schwartz, T.U., *Modularity within the architecture of the nuclear pore complex*. *Current opinion in structural biology*, 2005. **15**(2): p. 221-226.
87. *Nuclear mRNA Transport*. [cited 2016 June 2016]; http://mol-biol4masters.masters.grkraj.org/html/Ribose_Nucleic_Acid6-Nuclear_mRNA_Transport.html.
88. Jamali, J. and J. Wood. *Mixed-mode through-thickness fracture of polymer matrix composites*. in *Proceedings of the 19th International Conference on Composite Materials (ICCM 19)*. Montreal (Canada). 2013.
89. Liu, A.F., *Mechanics and mechanisms of fracture: an introduction*. 2005: ASM International.
90. van Oers, M.M., *Opportunities and challenges for the baculovirus expression system*. *Journal of invertebrate pathology*, 2011. **107**: p. S3-S15.
91. Hitchman, R.B., et al., *Baculovirus as vectors for human cells and applications in organ transplantation*. *Journal of invertebrate pathology*, 2011. **107**: p. S49-S58.
92. Rychlowska, M., et al., *Application of baculovirus-insect cell expression system for human therapy*. *Current pharmaceutical biotechnology*, 2011. **12**(11): p. 1840-1849.
93. Rivera-Gonzalez, G.C., et al., *Baculoviruses as gene therapy vectors for human prostate cancer*. *Journal of invertebrate pathology*, 2011. **107**: p. S59-S70.
94. Hitchman, R.B., et al., *Optimizing the baculovirus expression vector system*. *Methods*, 2011. **55**(1): p. 52-57.
95. Au, S., S. Cohen, and N. Panté, *Microinjection of *Xenopus laevis* oocytes as a system for studying nuclear transport of viruses*. *Methods*, 2010. **51**(1): p. 114-120.